EXPERIMENTAL STUDIES OF LIQUEFACTION AND DENSIFICATION OF LIQUID OXYGEN

by

JONATHAN KOERT PARTRIDGE
B.S. Tennessee Technological University, 2003

A thesis submitted in partial fulfillment of the requirements
for the degree of Master of Science in Mechanical Engineering
in the Department of Mechanical, Materials, and Aerospace Engineering
in the College of Engineering and Computer Science
at the University of Central Florida
Orlando, Florida

Fall Term
2010

ABSTRACT

The propellant combination that offers optimum performance is very reactive with a low average molecular weight of the resulting combustion products. Propellant combinations such as oxygen and hydrogen meet the above criteria, however, the propellants in gaseous form require large propellant tanks due to the low density of gas. Thus, rocketry employs cryogenic refrigeration to provide a more dense propellant stored as a liquid. In addition to propellant liquefaction, cryogenic refrigeration can also conserve propellant and provide propellant subcooling and propellant densification. Previous studies analyzed vapor conditioning of a cryogenic propellant, with the vapor conditioning by either a heat exchanger position in the vapor or by using the vapor in a refrigeration cycle as the working fluid. This study analyzes the effects of refrigeration heat exchanger located in the liquid of the common propellant oxidizer, liquid oxygen.

This study predicted and determined the mass condensation rate and heat transfer coefficient for liquid oxygen.

ACKNOWLEDGEMENTS

The author acknowledges Jeff Tuttle, Kevin Jumper, Brian Hunter, Matt Nugent, Gary Wall, Jeff Wall, Bill Notardonato, and Wesley Johnson for their contributions to the design, operation, management, and consultation of IRAS data analysis and evaluation.

TABLE OF CONTENTS

LIST OF FIGURES

LIST OF TABLES

LIST OF ACRONYMS AND SYMBOLS

Acronyms

ARC	NASA – Ames Research Center
GHe	Gaseous Helium
GN_2	Gaseous Nitrogen
GO_2	Gaseous Oxygen
IRAS	Integrated Refrigeration and Storage
KSC	NASA – Kennedy Space Center
LC	Launch Complex
LN_2	Liquid Nitrogen
LO_2	Liquid Oxygen
MAWP	Maximum Allowable Working Pressure
MRI	Magnetic Resonance Imaging
NASA	National Aeronautics and Space Administration
NASP	National Aerospace Plane
ZBO	Zero Boil-off

Equations

A		area (m^2)
	A_f	surface area of a single fin (m^2)
	A_p	corrected fin profile area – $A_p = L_c t$ (m^2)
	A_s	surface of liquid in IRAS (m^2)
	A_t	total surface area for a cylindrical finned heat exchanger (m^2)
a		ratio of overall speed to molecular characteristic velocity ( )
C		constant
	C_z	constant for bubble velocity ( )
	C_D	constant for
c_p		specific heat capacity (J/kg·K)
D		diameter of tubing (m)
	D_n	diameter of nozzle (m)
	D_d	diameter of bubble at departure from nozzle (m)
	D(t)	bubble radius as a function of time as the bubble rises to the surface (m)
f		friction factor ( )
f_b		bubble departure frequency (1/s)
Fo		Fourier number (unitless)
	Fo_0	Fourier number based on bubble departure diameter $\mathrm{Fo}_0 = \frac{\alpha\, t}{D_d^2}$
G		mass flux ($kg/m^2 \cdot s$)
	G_{COND}	conduction mass flux ($kg/m^2 \cdot s$)
g		gravitational constant (m/s^2)
	g_c	($32.2\ lb_m \cdot ft/lb_f \cdot s^2$)
Gr		Grashoff number ( )
H		height (m)
h		convection heat transfer coefficient ($W/m^2 \cdot K$)
	h_{CC}	condensation convection heat transfer coefficient ($W/m^2 \cdot K$)
	h_{EC}	external convection heat transfer coefficient ($W/m^2 \cdot K$)
	h_{IC}	internal convection heat transfer coefficient ($W/m^2 \cdot K$)
	h_{mic}	microscopic convective coefficient due to nucleate boiling ($W/m^2 \cdot K$)

	h_{mac}	macroscopic convective coefficient due to bulk convection (W/m²·K)
h_{lv}		latent heat (J/kg)
	h'_{lv}	modified latent heat (J/kg)
Ja		Jakob number defined by $\mathrm{Ja} = \frac{\rho_l c_p (T_{sat} - T_l)}{\rho_v h_{lv}}$ (unitless)
k		thermal conductivity (W/m·K)
	k_l	liquid thermal conductivity (W/m·K)
	k_{PTFE}	thermal conductivity of polytetrafluorethylene (W/m·K)
	k_{SS}	thermal conductivity of stainless steel (W/m·K)
	k_v	vapor thermal conductivity (W/m·K)
L		length of tube (m)
	L_c	corrected length – $L_c = L + t/2$ (m)
M		molecular weight (kg/mol)
m		mass (kg)
	$m_{b,cond}$	mass of bubble that condenses when rising through subcooled liquid (kg)
$\dot{m}$		mass flow rate (kg/s)
	$\dot{m}_{b,cond}$	mass condensation rate of bubble rising through subcooled liquid (kg/s)
	$\dot{m}_{GO_2}$	mass flow rate of gaseous oxygen entering IRAS dewar (kg/s)
N		number of fins ( )
Nu_D		Nusselt number ( )
q		heat transfer rate (W)
	q_r	radial heat transfer rate (W)
	q_t	heat transfer rate (W)
P		pressure (Pa = kg/m²)
	P_c	critical pressure (Pa)
	P_g	pressure of gas (Pa)
	P_{sat}	saturated pressure as a function of a given temperature (Pa)
	P_{ref}	reference pressure equivalent to 1,000,000 Pa (Pa)
	P_t	triple point pressure (Pa)
	P_v	vapor pressure as a function of temperature (Pa)
	P^*	dimensionless pressure ( )
Pr		Prandtl number ( )
R		thermal resistance (K/W)

	R_{tot}	total thermal resistance (K/W)
r		radius (m)
	r_{2c}	corrected fin radius – $r_{2c} = r_2 + t/2$, (m)
R_u		universal gas constant (J/mol·K)
Ra_D		Raleigh number ( )
Re		Reynolds number (unitless)
	Re_{b0}	Reynolds number based on bubble departure diameter $Re_{b0} = \frac{\rho_l u_b D_d}{\mu_l}$
	Re_δ	Reynolds number for condensate flowing down exterior tube wall ( )
	Re_l	liquid Reynolds number ( )
	Re_{tp}	two phase Reynolds number ( )
S		suppression factor ( )
T		temperature (K)
	T_c	critical temperature (K)
	T_g	temperature of gas (K)
	T_{sat}	Saturation temperature (K)
	T_s	Surface temperature (K)
	T_t	triple point temperature (K)
	T_w	wall temperature (K)
t		time (s)
	t_r	time for bubble to rise from nozzle to liquid surface (s)
u		velocity (m/s)
	u_b	bubble velocity (m/s)
	u_T	terminal bubble velocity (m/s)
V		volume (m^3)
v		specific volume (m^3/kg)
	v_{lv}	difference in the specific volume of the liquid phase and vapor phase
X_{tt}		Martinelli parameter ( )
x		mole fraction ( )

Equations – Greek Symbols

α	thermal diffusivity (m^2/s)	
α	void fraction ( )	
β	ratio of bubble diameter, D(t), to the bubble departure diameter, D_d, (unitless)	
γ	specific heat ratio ( )	
δ	film thickness layer (m)	
$\Gamma(a)$		
η_f	single fin efficiency ( )	
μ	viscosity (kg/m·s)	
	μ_l	liquid viscosity (kg/m·s)
θ_b	temperature difference between heat exchanger base and bulk fluid (K)	
π	constant of circumference to diameter ratio of a circle – 3.14159	
ρ	density (kg/m^3)	
	ρ_f	liquid density (kg/m^3)
	ρ_g	vapor density (kg/m^3)
	ρ_{fg}	difference in liquid density and vapor density (kg/m^3)
σ	condensation and evaporation coefficient	
	σ_c	condensation coefficient
	σ_e	evaporation coefficient
σ	surface tension (N/m)	

Measurement Units

°C	Degrees Celsius	
J	Joule	
K	Kelvin	
kg	kilogram	
m	meter	
mol	mole	
N	Newton	
Pa	Pascal	
	Paa	Pascal - atmosphere
	Pag	Pascal - guage
ppm	Parts per million	
psi	Pound force per square inch	
	psia	pound force per square inch - atmosphere
	psig	pound force per square inch - gauge
s	second	
sLm	standard Liters per minute	
W	Watt	

CHAPTER ONE: INTRODUCTION

Cryogenic Background

Refrigeration is an important technology that sustains our society and economy. One of the initial uses of refrigeration preserved food, enabling the economic shipment of food from source to market. Today refrigeration provides many uses, ranging from conditioning the air within buildings and vehicles to cooling the magnets in medical instruments, such as the Magnetic Resonance Imaging (MRI). A special branch of refrigeration emerged in the nineteenth century known as cryogenics, defined as temperatures below -150°C.

Prior to the 1840s, mechanical refrigeration by compression and isenthalpic expansion could condense most elements and compounds; the remaining elements and compounds were termed "permanent gases". After 1875 refrigeration technology entered the cryogenic temperature range when scientists condensed air. Scientists condensed the remaining "permanent gases" one by one until Onnes finally condensed helium in 1908. Cryogenic refrigeration was confined to the bench top until the early 1900s when Linde developed an economic process on an industrial scale to purify oxygen by the cryogenic distillation of air [1]. Eventually rocketry would take advantage of the industrial scale production of liquid oxygen and other cryogenic propellants and pressurants.

In 1903 the early Russian rocket scientist, Tsiolkovsky, predicted the velocity needed to reach orbit about the Earth and suggested that liquid oxygen and liquid hydrogen offered optimum performance to achieve the orbital velocity [2]. The American, Goddard, launched the first liquid fueled rocket using the cryogenic oxidizer, liquid oxygen, with ethanol in 1926. The Americans also developed the first fully cryogenic rocket engine, powered by liquid oxygen and liquid hydrogen, in 1963 [3]. Today, the hydrogen-oxygen rocket engine remains a common propellant combination, used by the nations of Japan, Europe, India, China, Russia, and the United States [1]. Since the beginning of the space age, rocket scientists have looked at cryogenic refrigeration for thermal control, to increase the propellant density and conserve propellant. Figure 1 shows the rocketry applications for cryogenic refrigeration.

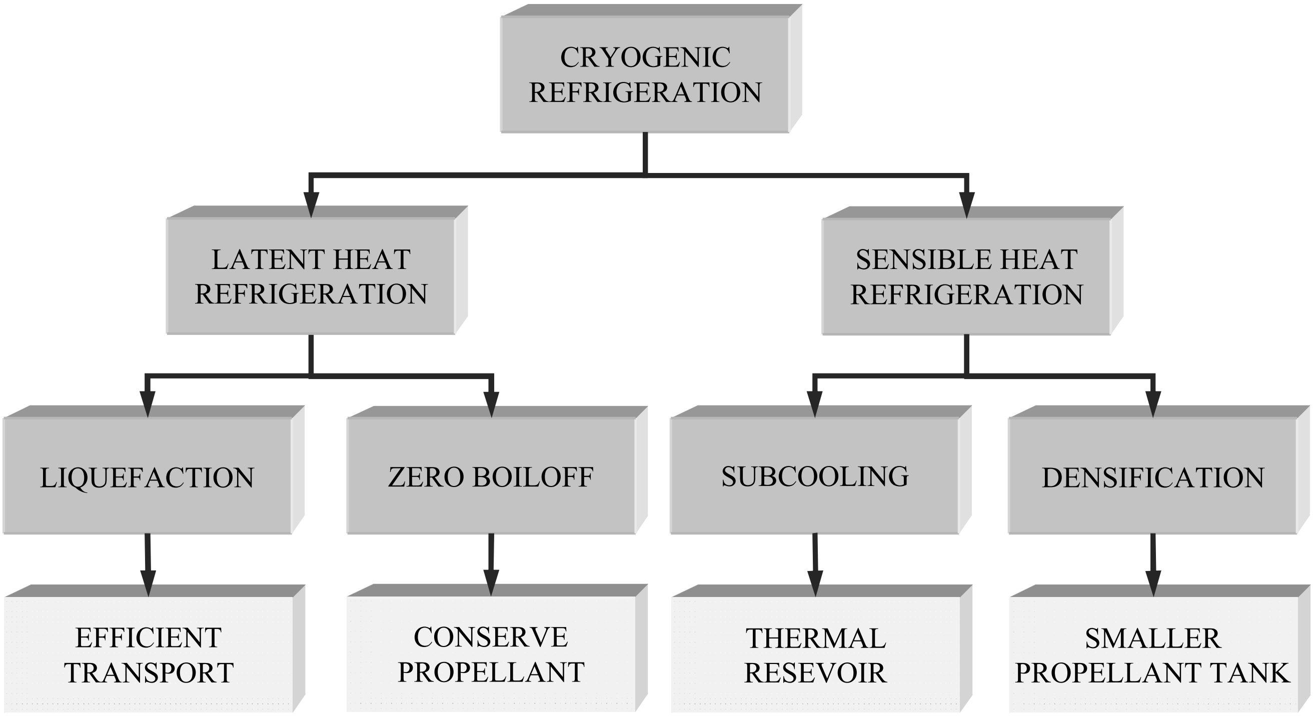

Figure 1: Cryogenic Refrigeration and Rocketry Use

Liquefaction

Liquefaction of propellant gases typically occurs at the source plant offers efficient storage and transportation of propellant gases. For instance, liquid oxygen is approximately five times denser than gaseous oxygen transported at the typical industrial pressure of 2400 psi. Accounting for the thicker walls of the pressure vessels on the compressed gas trailer when compared to a cryogenic vessel, six compressed gas trailers deliver the same amount of oxygen as a single delivery of liquid oxygen. Within the rocket, pump-fed systems pressurize the cryogen to high pressures before injection into the rocket's combustion chamber. Turbo pumps offer increased efficiency in both pressurization and flow of a cryogenic liquid as opposed to gas compressor efficiency.

A typical liquefier uses some variation of the Claude cycle, which compresses the fluid and subsequently expands the fluid both, isentropically and isenthalpically after removing the heat of compression. An expansion engine, such as a turbine, accomplishes isentropic expansion, while an expansion valve, also known as a Joules-Thomson valve, accomplishes isenthalpic expansion [4].

Currently, no liquefaction occurs at the launch pad of any United States launch facility, since the cryogenic propellant required for launch is delivered as a liquid to storage tanks near the launch pad. However, space missions to other surfaces with in-situ resource utilization, liquefaction at the launch site will be necessary. Proposed methods of propellant liquefaction on other planetary surfaces utilize the compression – heat rejection – expansion methods, such as the Sterling cycle refrigerator [5].

Zero Boil-off

Because the temperature difference between the ambient temperature surrounding a cryogenic vessel and the temperature of the cryogen, heat transfers from the ambient to the cryogen and the cryogen eventually evaporates from the cryogenic vessel. Early cryogenic scientist/engineer, James Dewar, developed insulated cryogenic vessels, consisting of one glass flask inside of another glass flask. Dewar evacuated the annular space between the two glass flasks to inhibit conductive and convective heat transfer, and Dewar silvered the glass between the glass flasks to inhibit radiation heat transfer. Currently, stainless steel replaced the glass as the vessel material and perlite powder or multi-layer insulation replaced the silvering of vessel material. Recent studies show that more efficient annular materials exist, but the economics questions the employment of the annular material. Nevertheless, these vessels are termed dewars, named after James Dewar.

Insulation attempts to reduce heat entering the cryogenic vessel from the ambient, however, no insulation stops heat from entering the cryogenic vessel. Thus, heat removal from the dewar remains the only method to maintain the dewar contents at cryogenic temperature. Evaporation of the cryogen removes heat from the dewar through latent heat, but this method expends a portion of the cryogen in order to maintain the temperature. Active cooling employs refrigeration to remove the heat that enters the vessel and requires energy, but conserves the cryogen by prohibiting cryogen evaporation or zero boil-off (ZBO). Economic analysis determines the most beneficial type of insulation for ground support system, while space missions consider overall payload weight and length of service to determine insulation and active cooling requirements.

Zero Boil-off Benefits in Rocketry

Space missions consider ZBO concepts for propellant management and cryogenic coolant. Typically, hypergolic propellants are used on long-term or deep space missions due to the storability of the hypergolic propellants. Although cryogenic propellants offer higher performance than hypergolic engines, no cryogenic propellant will remain through the duration of the long-term mission unless the spacecraft employs a zero boil-off concept. Simple analysis shows that any mission longer than 60 days for liquid hydrogen or 10 days for liquid oxygen benefit from ZBO [6]. Some telescopic instruments aboard spacecraft use cryogens, such as liquid helium, to cool the instruments to reduce radiation noise, however, the mission typically lasts three months because the helium warms to a temperature that can no longer shield radiation noise.

Zero Boil-off Challenges in Rocketry

No technical challenges exist to employ ZBO concepts for ground storage tanks, however, two technical challenges exist for ZBO in space: heat rejection and fluid thermal stratification. A spacecraft relies on radiation heat transfer to reject any heat that an onboard cryogen (1) absorbs from other planetary or stellar bodies through radiation heat transfer or (2) absorbs because of spacecraft electrical power generation through conduction heat transfer. Microgravity, as experienced in space, limits natural convection. Without convection, a spacecraft's cryogenic vessel can experience localized heating leading to complete vaporization in the immediate vicinity of heating even though the mean bulk temperature may remain below the saturation temperature. Thus, other means of convection, such as fans, magnets, or artificial gravity, provide the heat transfer needed to cool the cryogen evenly while in space. Numerous studies have addressed these issues [7] [8].

Zero Boil-off History in Rocketry

Earth Ground Systems – In the years prior to the Space Shuttle Program, NASA studied concepts to capture the boil-off from the two liquid hydrogen storage tanks at Launch Complex 39 (LC-39) at the Kennedy Space Center. At that time approximately 400 gallons of liquid hydrogen evaporated from each of the KSC storage tanks every day. Two studies in the late 1970s suggested to place a cryocooler in the storage tank's existing manhole, located at the top of storage tank, to condense the ullage vapor, maintaining the storage tank at a constant pressure [9][10]. Later in the 2006, Ames Research Center (ARC) analyzed the LC-39 cryogenic tanks for use in the Constellation Program. ARC concluded that a refrigeration system on the LC-39 tanks would be technically viable, however, the study questioned the economic benefits [11].

Passive In-Space Zero Boil-off – While in space, heat is transferred to the cryogenic propellant tank by two modes, conduction and radiation. The Sun, planets, and other stellar bodies transfer heat by radiation to the spacecraft. Also, the spacecraft itself conducts heat, that it absorbs from stellar bodies and generates for spacecraft power, toward the cryogenic propellant tank. Although most spacecraft with cryogenics aboard employ radiation shields and insulation supports to protect the cryogenic propellant tanks from both modes of heat transfer, passive zero boil-off rely exclusively on radiation shields and insulation supports to conserve cryogenic propellant. Passive zero boil-off is possible for missions beyond the orbit of Mars [12] and for special applications such as the James Webb Space Telescope, which will be deployed to the L2 point where Earth and Sun are aligned so that a single radiation shield can protect the telescope from both bodies[13].

Active In-Space Zero Boil-off – As mentioned above, most spacecraft employ insulation techniques to reduce heat transfer while in space. If the insulation is insufficient to negate the overall heat transfer to the cryogenic propellant tank, active cooling can be employed to offset the heat into the cryogenic propellant tank. In the past 20 years, approximately twenty cryocoolers have been launched aboard NASA satellites. The cyrocoolers operated in a temperature range of 55K to 150K, with the exception of the 20K cryocooler aboard the Plank spacecraft. More recent cyrocooler designs hope to achieve 6K operational temperatures. [14]

Subcooling

Removing sensible heat from the liquid reduces the temperature of a liquid. Also, the vapor pressure of a liquid decreases as the liquid temperature decreases. The saturated temperature occurs at the temperature at which the liquid vapor pressure equals the system pressure. To subcool a liquid, the vapor pressure must be lowered below the system pressure, or stated another way, the temperature must be lowered below the saturated temperature. For further liquid subcooling, the liquid approaches the melting line. A propellant, at the melting line, can exist as a liquid, solid , or slush defined as a mixture of liquid and solid.

Subcooling Benefit in Rocketry

A subcooled propellant provides cooling, or a thermal sink, to a rocket with a small change in volume in the propellant. The amount of cooling a subcooled propellant can store depends on the specific heat of the propellant and the temperature difference between the subcooled liquid temperature and the saturation temperature.

Subcooling History in Rocketry

The National Aerospace Plane (NASP) intended to use slush hydrogen as a propellant. NASA designed the NASP to be capable of withstanding the extreme heat caused by hypersonic velocity . The slush hydrogen was intended to provide cooling to the plane structure prior to combustion.

Densification

As with subcooling, the removal of sensible heat from a liquid increases the density of the liquid. The liquid density depends on temperature alone since a liquid is considered incompressible. Thus, liquid density continually increases from the critical point to triple point regardless of level of subcooling. However, NASA typically stores propellants as single component-two phase with the ullage and liquid at saturated conditions.

Density Benefit in Rocketry

Propellant comprises the majority of a rocket's weight just prior to launch, with rocket engines, propellant tanks, and payload make up the remaining weight. In order to maximize the payload weight, rocket scientists attempt to minimize the propellant tank weight. Altering the tank material is one method of reducing the propellant tank weight. NASA reconfigured the Space Shuttle's External Tank three times throughout the history of the Space Shuttle Program to reduce weight. Propellant densification, or increasing the density of the propellant, offers another method of reducing the overall rocket weight by making the tank smaller.

Density Challenges in Rocketry

If the propellant refrigeration occurs on the earth's surface and the ullage is not pressurized with a non-condensable, the propellant tank pressure becomes sub-atmospheric, which produces two challenges: (1) structural integrity of the propellant tank as well as (2) possible atmospheric intrusion into the propellant tank. If the intent of refrigeration is to maintain a consistency of slush propellant, further difficulty arises as the liquid temperature approaches the propellant melting line. Because refrigeration equipment would add weight to a launch vehicle, propellant densification occurs away from the launch vehicle. Difficulty arises when maintaining the propellant in a densified state during transfer from the refrigeration equipment to the launch vehicle.

Densification History in Rocketry

The sub-orbital launch vehicle, X-15, from the 1960s utilized a passive system of liquid oxygen densification by replenishing the liquid oxygen from the B-52 carrier aircraft. As the B-52 and X-15 rose to altitude, the liquid oxygen boiling point reduced as the ambient pressure lowered, thus, the bulk liquid oxygen temperature decreased resulting in a densified liquid oxygen. The X-33 was intended to use both, densified liquid oxygen and liquid hydrogen, to accomplish a single stage to orbit vehicle. Several ground support systems to provide propellant densification were proposed in the late 1990s to support X-33 flights. One used a sub-atmospheric liquid nitrogen as the working fluid [15] while another proposal bubbling liquid hydrogen through a liquid nitrogen working fluid [16]. The Space Shuttle Program studied densified propellants in the mid 1990s and identified the changes needed to launch the STS with densified propellants; the result was considered too expensive to retrofit the current infrastructure, but recommended looking at densified propellants for a new program [17].

Purpose of This Work

For ground systems, the argument for cryogenic refrigeration system becomes purely economic. The economic trade for propellant ZBO, propellant subcooling, and propellant densification depends on the cost of propellant and rocket specification and performance versus the operational and capital costs of a cryogenic refrigeration system. Propellant liquefaction may occur at the launch site on other planetary surfaces, but will probably occur away from the launch site for future NASA launch concepts.

Previous concepts use propellant ullage vapor as working fluid to produce refrigeration, which introduces the possibility of contaminating the propellant. Other concepts employed a heat exchanger or cold head within the ullage to control dewar pressure. This paper studies the effect of employing a heat exchanger or cold head beneath the liquid surface. Because the location of the heat exchanger or cold head is inside the tank, this type of configuration is intended for the ground storage tanks on earth or other planetary surfaces. Specifically, this paper investigates the heat and mass transfer at the vapor-liquid interface as a result of cooling the liquid.

CHAPTER TWO: LITERATURE SEARCH

Condensation

Condensation occurs by four different methods – film condensation, dropwise condensation, homogeneous condensation and direct contact condensation. Film condensation and dropwise condensation occur at a solid surface and depend on surface conditions. Film condensation occurs on a surface that promotes liquid wetting, thus, a thin film of liquid covers the solid surface. Dropwise condensation occurs on a solid surface that inhibits liquid wetting, therefore drops or beads of liquid form over the solid surface. Homogeneous condensation occurs when vapor condenses in the gas phase and the condensation remains suspended in the gas phase. Direct contact condensation occurs when vapor condenses into a body of liquid. Vapor can come in direct contact with a liquid by either the vapor directly above a liquid or by vapor bubbles rising through a body of liquid. The type of condensation investigated in the IRAS experiment is direct contact condensation [18]. Models below predict heat transfer coefficient both types of direct contact condensation.

Direct Contact Condensation Models

Direct Contact Condensation by Ullage Collapse

Due to safety concerns, vapor exists above a layer of cryogenic liquid, known as ullage. As the liquid achieves a subcooled state, the pressure of the ullage above the liquid decreases. In accordance with the gas laws, the decrease in ullage pressure can be attributed to a (1) decrease in ullage temperature, (2) an increase in ullage volume due to liquid densification, or (3) a decrease in ullage mass due to ullage condensation. Direct Contact Condensation by Ullage Collapse refers to the ullage condensation on a liquid surface and is (1) modeled using kinetic theory and (2) modeled the liquid as a flat, horizontal, cold plate.

Kinetic Theory – Condensation heat transfer coefficient has been estimated with the use of kinetic theory. Kinetic theory characterizes the random motion of molecules using statistical mechanics. Equation 1 and Equation 2 are used to predict the mass condensation rate and heat transfer coefficient, respectively [19].

$$G_{COND} = \left(\frac{M}{2\pi R_u T}\right)^{\frac{1}{2}} \left[P_{sat} - P_g\right]$$

Equation 1

$$h = \left(\frac{M}{2\pi R_u T}\right)^{\frac{1}{2}} \frac{h_{lv}^2}{T\, v_{lv}}$$

Equation 2

Equation 1 was modified by applying correction factors to both individual condensation and evaporation mass flux equations. Both mass flux equations are combined into Equation 3, with supporting definitions provided by Equation 4 and Equation 5. No additional heat transfer coefficient is predicted using Equation 3.

$$G_{COND} = \left(\frac{M}{2\pi R_u T}\right)^{\frac{1}{2}} \left[\Gamma(a)\sigma_c P_v - \sigma_e P_g\right]$$

Equation 3

$$\Gamma(a) = \exp(-a^2) + a\sqrt{\pi}[1 + \mathrm{erf}(a)]$$

Equation 4

$$a = \frac{G_{\mathrm{COND}}}{P_g} \sqrt{\frac{R\ T}{2\ M}}$$

Equation 5

Cold Plate Model – The cold plate model assumes the heat from the enthalpy of condensation is transferred though the liquid to the cold plate. The heat transferred through the liquid is by thermal conductance and neglects convective heat transfer. The thermal resistance increases with time because the height, or thickness, of the liquid increases as the ullage condenses. Equation 6 and Equation 7 give the mass condensation rate and the heat transfer coefficient, respectively, for the cold plate analysis, as derived in APPENDIX D.

$$G_{\mathrm{COND}} = k_l(T_{sat} - T_s) \sqrt{\frac{\rho_l}{h_{lv}\left[2\ k_l\ (T_{sat} - T_s)\ t + \delta_i^2\ h_{lv}\ \rho_l\right]}}$$

Equation 6

$$h = k_l \sqrt{\frac{h_{lv}\ \rho_l}{2\ k_l\ (T_{sat} - T_s)\ t + \delta_i^2\ h_{lv}\ \rho_l}}$$

Equation 7

Direct Contact Condensation by Bubble Collapse

Direct contact condensation of a bubble rising through a layer of subcooled liquid is a complex subject. Typically, the bubbles are injected into the liquid by a nozzle and the bubble separates from the nozzle at a specific diameter, called the bubble departure diameter. Equation 8 estimates the bubble departure diameter [20].

$$D_{b,d} = \sqrt[3]{\frac{6\ \sigma\ D_n}{\rho_{fg}\ g}}$$

Equation 8

The diameter of the bubble continually decreases as the bubble rises through the subcooled liquid because of bubble vapor cooling. The vapor within the bubble cools as the bubble transfers heat to the subcooled liquid, which reduces the volume of the bubble according to the gas laws and ultimately condenses portions of the bubble. Equation 9 shows the rate at which the bubble diameter decreases as with time [21].

$$\beta = \frac{\mathrm{D_b(t)}}{\mathrm{D_{b,d}}} = \left(1 - \frac{3}{\sqrt{\pi}}\,\mathrm{Ja}\,\sqrt{\mathrm{Re_{bo}}}\,\mathrm{Pr}^{\frac{1}{3}}\,\mathrm{Fo_o}\right)^{\frac{2}{3}}$$

Equation 9

Although literature has suggested that a bubble rising through subcooled liquid goes through an acceleration and deceleration phase [22], this study assumes constant vertical velocity. Equation 10 [23] and Equation 11 [24] calculates the vertical bubble velocity and terminal bubble velocity, respectively.

$$\mathrm{u_b} = \frac{\mathrm{C_z}}{1-\alpha}\left(\frac{\mathrm{g}\,\sigma\,\rho_{\mathrm{fg}}}{\rho_{\mathrm{f}}^{2}}\right)^{\frac{1}{4}}$$

Equation 10

$$\mathrm{u_T} = \sqrt{\frac{2.14\,\sigma_{\mathrm{L}}}{\rho_{\mathrm{l}}\mathrm{D}} + 0.505\,\mathrm{g}\,\mathrm{D}}$$

Equation 11

As mentioned above, the bubble collapses as it rises to the surface, partly due to condensation of the vapor within the bubble. The mass of the vapor that condenses while the bubble rises is dependent on the heat transfer rate and the residence time the bubble spends within the subcooled liquid. Given the above constant bubble rise velocity assumption, Equation 12 calculates the residence time of the bubble within the subcooled liquid.

$$t_r = \frac{H}{u_b}$$

Equation 12

Equation 13 calculates the mass that condenses from a single spherical bubble.

$$m_{b,cond} = \rho_v \frac{4\pi}{3}\left(\frac{D_{b,d}}{2}\right)^3 - \rho_v \frac{4\pi}{3}\left(\frac{D_{t_r}}{2}\right)^3$$

Equation 13

However, during the proposed IRAS test matrix as outlined in the following chapter, a steady stream of bubbles depart from the nozzle instead of a single bubble. The frequency at which a bubble departs the nozzle depends on the mass flow rate of the gas flowing through the nozzle and the mass of the bubble at departure. Equation 14 and Equation 15 calculate the bubble departure frequency and mass condensation rate of the bubble. APPENDIX D shows the derivation for Equation 14 and Equation 15.

$$f_{b,d} = \frac{6\,\dot{m}_{GO_2}}{\pi\,\rho_v\,D_{b,d}^3}$$

Equation 14

$$\dot{m}_{b,cond} = \dot{m}_{GO_2}\left(1 - {\beta_{t_r}}^3\right)$$

Equation 15

Equation 16 calculates the instantaneous Nusselt number [21].

$$Nu_c = \frac{1}{\sqrt{\pi}}\sqrt{Re_b}\,Pr^{\frac{1}{3}}$$

Equation 16

Equation 17 calculates the average heat transfer coefficient by averaging the Nusselt number at the time of departure and at the moment the bubble reaches the surface.

$$h_{avg} = \frac{k_l}{2\sqrt{\pi}}\sqrt{Re_{b,d}}Pr^{\frac{1}{3}}\left(\frac{\beta_{t_r}+1}{\beta_{t_r}}\right)$$

Equation 17

Previous IRAS Work

The Integrated Refrigeration and Storage (IRAS) system is a dewar with a large flanged connection at the top of the dewar. The large flanged connection allows instrumentation cables and fluid connections pass from the inside of the dewar to the outside. The fluid connections are intended for liquid nitrogen coolant to flow through a heat exchanger, which is intended to simulate the cold head of a Brayton cycle cryocooler. The flange connection allows coldhead height to be altered. The following chapter provides additional details of the IRAS system and supporting equipment.

Eden Cryogenics delivered the IRAS to KSC in the summer of 2008. Over the next nine months, the IRAS was cleaned to oxygen cleanliness specifications, integrated with the rest of the test apparatus, and functionally tested with liquid nitrogen. The liquid nitrogen functional test determined the heat transferred to the IRAS wall from the ambient as 17.5W [25].

Following the liquid nitrogen functional test, ZBO experimentation began with liquid oxygen. Liquid oxygen filled the IRAS dewar to approximately 70% of full capacity. The heat exchanger was placed at the 10%, 40%, and 60% locations inside the IRAS dewar, and ZBO runs occurred at an IRAS dewar pressure of 3 psig, 5 psig, and 7 psig. Results from these experimental testing showed that the optimum heat exchanger location was at the 40% level [26].

CHAPTER THREE: METHODOLOGY

Experimental Setup

The Integrated Refrigeration and Storage (IRAS) dewar comprises the main test article for this study and is complimented by a liquid nitrogen supply, a gaseous oxygen supply, a nitrogen subcooler, numerous analyzers and sensors, and a data acquisition system. Figure 2 shows the simplified schematic of the experimental setup, while Table 1 shows the legend and component specification details.

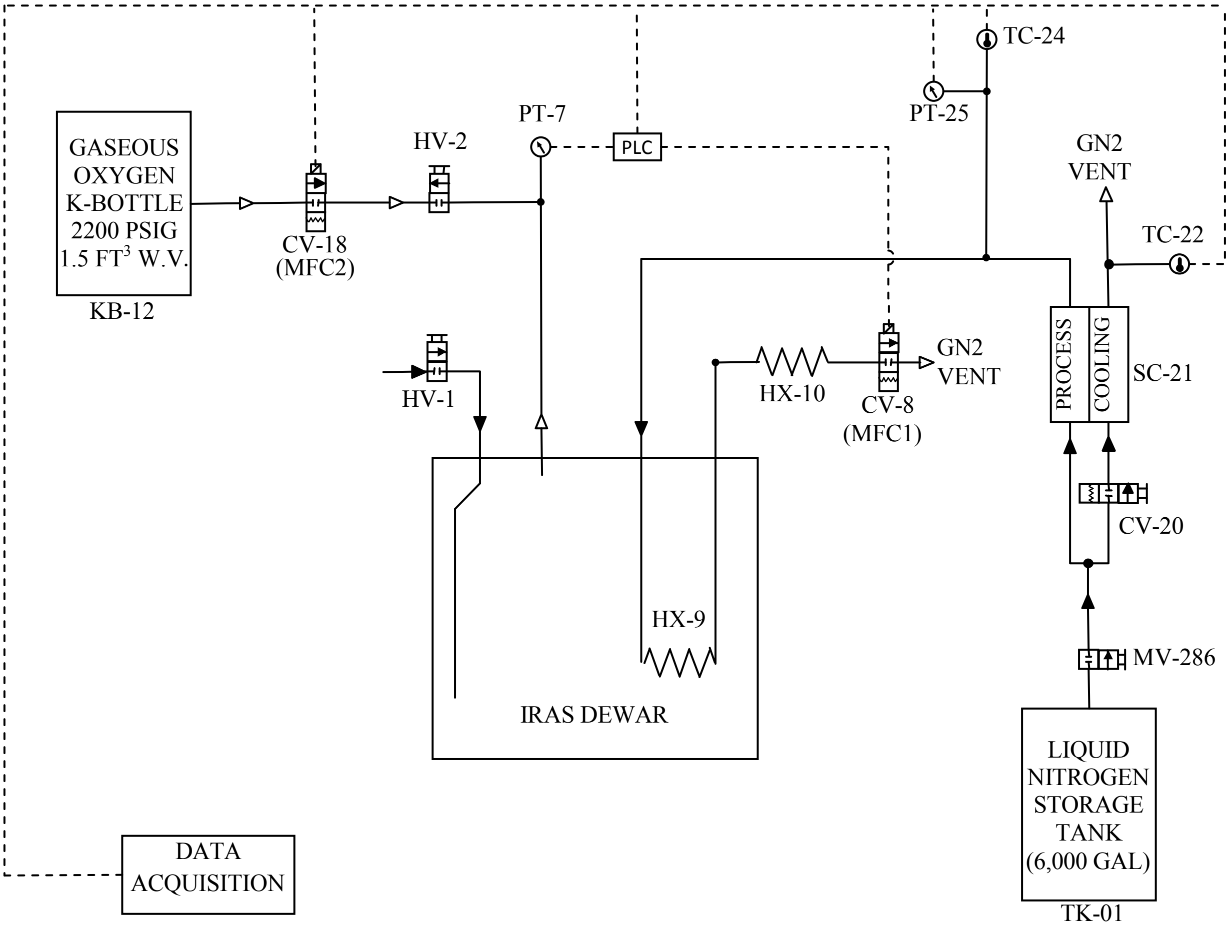

Figure 2: Experimental Setup - Simplified Process Instrumentation Diagram

Table 1: Experimental Setup - Simplified Process Instrumentation Diagram Legend

REFERENCE DESIGNATOR	DESCRIPTION
TK-01	Liquid Nitrogen Tank
HV-1	IRAS Dewar Inlet Valve
HV-2	IRAS Dewar Exit Valve
PT-7	IRAS Dewar Pressure Transducer
CV-8	IRAS Heat Exchanger Mass Flow Controller
HX-9	IRAS Heat Exchanger
HX-10	Coolant Ambient Heat Exchanger
KB-12	Gaseous Oxygen K-Bottle
CV-18	Gaseous Oxygen Mass Flow Controller
MV-286	Liquid Nitrogen Storage Tank Isolation Valve
CV-20	Subcooler Control Valve
SC-21	Subcooler
TC-22	Subcooler Cooling Fluid Exit Temperature Sensor
HX-23	Subcooler Cooling Fluid Ambient Heat Exchanger
TC-24	Subcooler Process Fluid Exit Temperature Sensor
PT-25	Subcooler Process Fluid Exit Pressure Transducer

APPENDIX B provides the detailed schematic and component specifications.

IRAS

The IRAS was custom built, consisting of a 400 liter dewar and a male bayonet. Both components were constructed of 304 stainless steel and double walled with a nominal vacuum of five microns of mercury within the annular space. Figure 3 shows a cross-sectional view of the IRAS.

Male Bayonet – The male bayonet connects to the IRAS dewar by a ten inch flange and all sensor and nitrogen fluid connections route through the male bayonet. Non-vacuum jacketed nitrogen fluid lines extend approximately one foot below the male bayonet and terminate with threaded fittings. Stainless steel tubing connect the terminated nitrogen fluid fitting to a copper heat exchanger. The copper heat exchanger is in the shape of a “U” and has annular fins. The

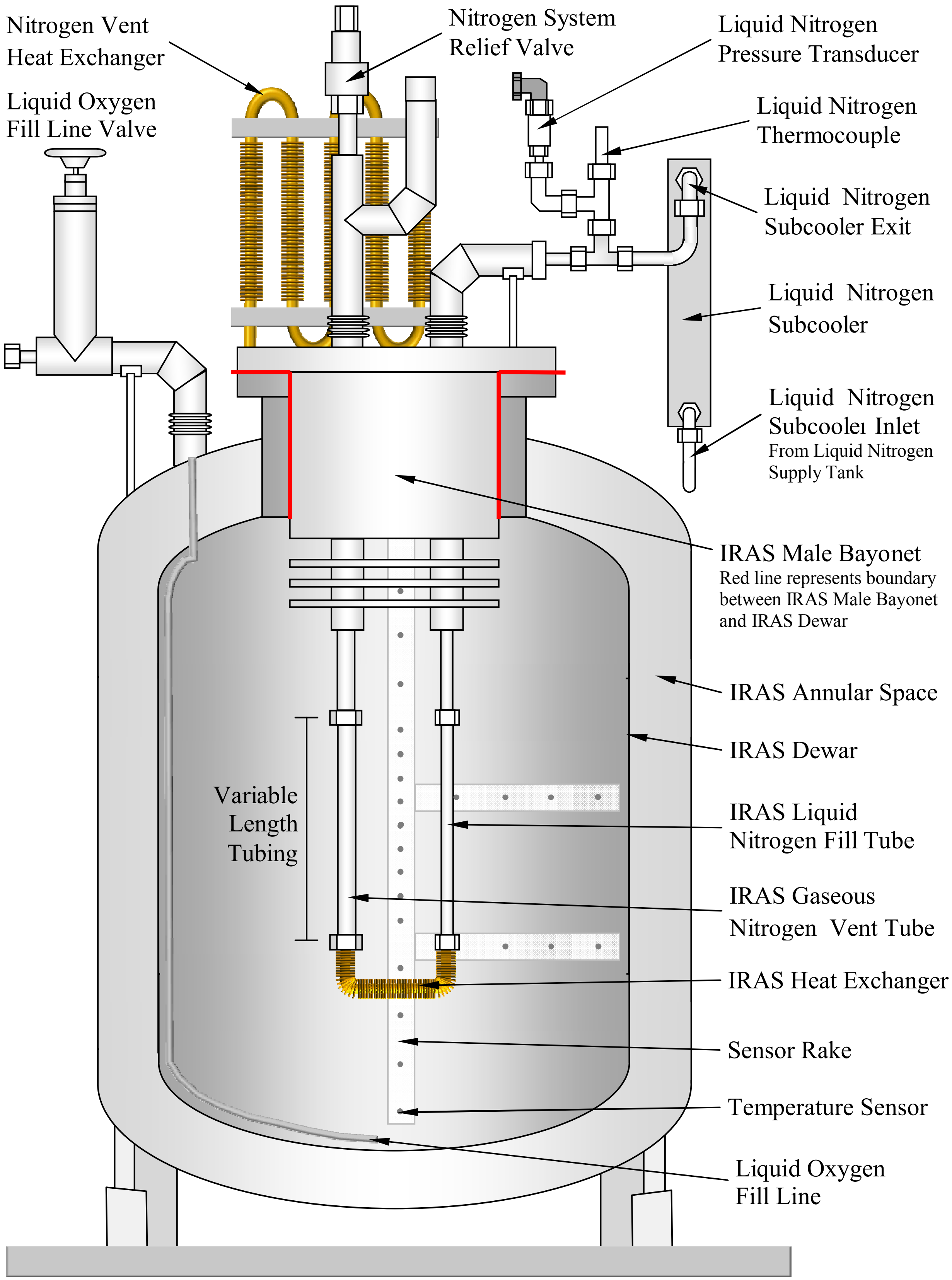

Figure 3: Cross-Section of IRAS Dewar and Male Bayonet

stainless steel tubing is insulated with Teflon tubing from the copper heat exchanger to the bottom of the vacuum insulated male bayonet. Heat transfer analysis of the Teflon insulated stainless steel tubing and copper heat exchanger is provided in APPENDIX A. Also attached to and extending below the male bayonet is a micarta instrumentation rake, where the internal temperature sensors, resistance temperature diodes, are strategically placed. The instrumentation rake extends to about six inches above the bottom of the IRAS dewar, with two horizontal rakes measuring the lateral temperature gradient.

IRAS Dewar – The IRAS dewar is an open container with a neck sized to accept the IRAS Male Bayonet. The liquid oxygen fill line and gaseous oxygen vent line are routed through the annular space, around the neck, and routed to the inside of the IRAS Dewar. Both lines have an external manual valve. Two pressure relief valves and a burst disc, which are located between the IRAS Dewar and the valve in the gaseous oxygen vent line, provide over-pressurization protection of the dewar. The IRAS dewar pressure is monitored by a pressure gauge and a pressure transducer, which is connected to the data acquisition system.

IRAS Support Equipment

Liquid Nitrogen Supply – A 6,000 gallon vertical tank provides liquid nitrogen to the IRAS dewar. The liquid nitrogen supply tank has a MAWP of 250 psi. The liquid nitrogen is procured to a military specification, MIL-PRF-27401E Grade B, which is an industrial grade nitrogen. The procurement requirements and laboratory analysis are found in APPENDIX C.

Gaseous Oxygen Supply – A 1.5 cubic foot water volume k-bottle provides gaseous oxygen to the IRAS dewar. The gaseous oxygen k-bottle has a MAWP of 2,200 psi. The gaseous oxygen is procured to a military specification, MIL-PRF-25508G Grade F, which is an electronic grade oxygen. The oxygen is 99.99% oxygen allowing a maximum impurity concentration of 100 parts per million. The procurement requirements and laboratory analysis is found in APPENDIX C. The gaseous oxygen pressure is regulated down to approximately 25 psig upstream of the mass flow controller.

Nitrogen Subcooler – The liquid nitrogen supply tank is operated at an elevated pressure in order to flow liquid nitrogen to the IRAS dewar. Once the liquid nitrogen supply tank reaches steady state conditions, the nitrogen becomes saturated at the elevated pressure, which corresponds to an elevated bulk liquid nitrogen temperature. As the liquid nitrogen flows to a lower pressure, a

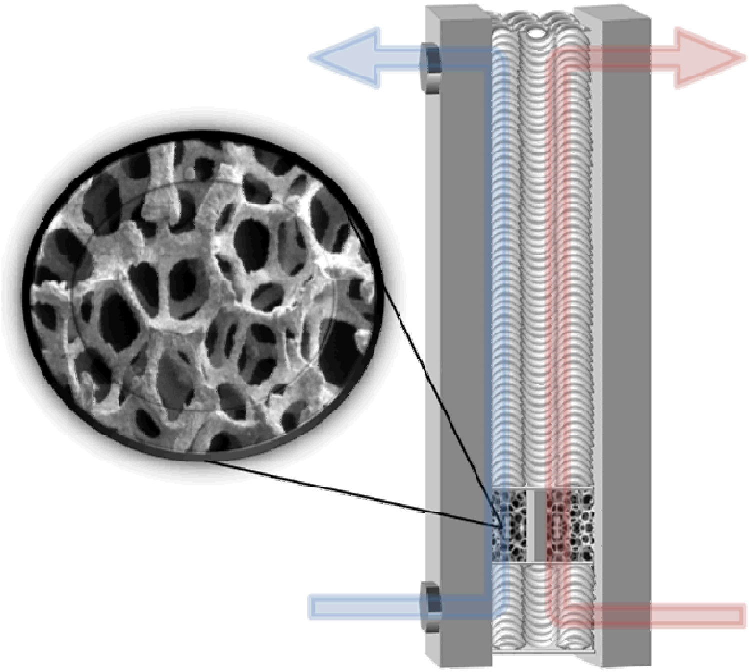

Figure 4: Liquid Nitrogen Subcooler

portion of the liquid nitrogen evaporates increasing the quality of the liquid nitrogen. Since the heat removed from the IRAS dewar is calculated by the latent heat of liquid nitrogen flowing through the IRAS, the validity of the calculation depends on the ability to obtain liquid nitrogen with no quality. The nitrogen subcooler is employed to subcool the liquid nitrogen and subsequently ensure the quality remains negligible.

The nitrogen subcooler is rectangular in shape, as shown in Figure 4, and constructed of aluminum, with the flow passages filled with aluminum metal foam. The nitrogen subcooler operates by splitting the liquid nitrogen into a process stream and a cooling stream. The cooling stream flow rate is regulated by a hand operated control valve located upstream of the subcooler. The cooling stream expands to atmospheric pressure downstream of the control valve, where the cooling stream boils at its normal boiling point providing cooling to the process stream. The process stream is maintained at pressure near the liquid nitrogen supply tank pressure, cooled in the subcooler, and enters the IRAS dewar. The nitrogen subcooler has experimentally provided approximately 11°C of subcooling in the mass flow rate range [27].

Flow Control Valves – The flow control valves measure and set the mass flow rates of the liquid nitrogen and the gaseous oxygen, which controls the cooling rate in the IRAS and measures the oxygen condensation rate. The nitrogen and oxygen flow control valves range from 0-20 standard liters per minute (sLm) and 0-100 sLm, respectively, with a tolerance of ±0.2 sLm and ±1 sLm, respectively.

Data Acquisition – The computer software, Labview, acquires data from the IRAS sensors or pressure transducers, thermocouples, resistance diodes, and mass flow controllers. The IRAS sensors are connected to field points and then to an ethernet switch. The ethernet switch is connected to the computer by a single RJ45 network cable. Labview records the signals from the pressure and temperature sensors and records and controls the mass flow controllers.

Test Configurations

The Integrated Refrigeration and Storage (IRAS) dewar is designed to measure the energy flow in a cryogenic storage system during active refrigeration. Figure 5 shows the energy balance about the IRAS, with the dotted line representing the control volume.

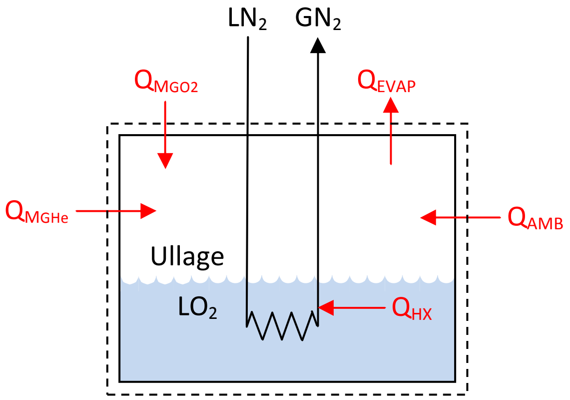

Figure 5: IRAS Energy Balance

Table 2: IRAS Energy Balance Definitions

Q_{MGO2}	Heat entering IRAS with gaseous oxygen
Q_{MGHe}	Heat entering IRAS with gaseous helium
Q_{HX}	Heat exiting IRAS through the heat exchanger
Q_{AMB}	Heat entering IRAS through dewar insulation
Q_{EVAP}	Heat exiting IRAS through evaporation

The energy balance shown in Figure 5 can be further subdivided into an energy balance about the liquid and an energy balance about the ullage. Figure 6 shows the subdivided IRAS energy balances.

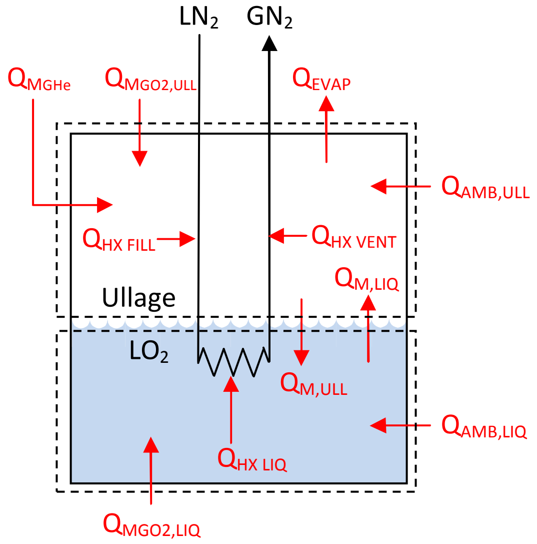

Figure 6: Subdivided IRAS Energy Balance

Table 3: Subdivided IRAS Energy Balance Definitions

$Q_{MGO2,ULL}$	Heat entering ullage with incoming gaseous oxygen
$Q_{MGO2,LIQ}$	Heat entering liquid with incoming gaseous oxygen
Q_{MGHe}	Heat entering ullage with gaseous helium
Q_{EVAP}	Heat exiting the ullage through evaporation
$Q_{HX\ LIQ}$	Heat entering heat exchanger from liquid
$Q_{HX\ VENT}$	Heat entering heat exchanger vent line from ullage
$Q_{HX\ FILL}$	Heat entering the heat exchanger fill line from ullage
$Q_{AMB,ULL}$	Heat entering ullage through dewar insulation
$Q_{AMB,LIQ}$	Heat entering liquid through dewar insulation
$Q_{M,LIQ}$	Heat entering ullage from liquid mass evaporation
$Q_{M,ULL}$	Heat entering liquid from ullage mass condensation

The energy balance from both, Figure 5 and Figure 6, are defined by Equation 18 through Equation 20, where Equation 18 represents the total IRAS energy balance, while Equation 19 and Equation 20 represent the components of the IRAS energy balance, the ullage balance and liquid balance, respectively.

IRAS Heat Balance

$$Q_{AMB} + Q_{\dot{m}_{GO_2}} + Q_{\dot{m}_{GHe}} = Q_{EVAP} + Q_{HX}$$

Equation 18

Ullage Subdivided Heat Balance

$$Q_{AMB,ULL} + Q_{\dot{m}_{GO_2},ULL} + Q_{\dot{m}_{GHe}} + Q_{\dot{m}_{LIQ}} = Q_{EVAP} + Q_{\dot{m}_{ULL}} + Q_{HX\ FILL} + Q_{HX\ VENT}$$

Equation 19

Liquid Subdivided Heat Balance

$$Q_{AMB,LIQ} + Q_{\dot{m}_{GO_2},LIQ} + Q_{\dot{m}_{ULL}} = Q_{HX\ LIQ} + Q_{\dot{m}_{LIQ}}$$

Equation 20

Adding Equation 19 and Equation 20 gives Equation 18 with the following definitions:

$$Q_{AMB} = Q_{AMB,ULL} + Q_{AMB,LIQ}$$

Equation 21

$$Q_{\dot{m}_{GO_2}} = Q_{\dot{m}_{GO_2},ULL} + Q_{\dot{m}_{GO_2},LIQ}$$

Equation 22

$$Q_{HX} = Q_{HX\ LIQ} + Q_{HX\ FILL} + Q_{HX\ VENT}$$

Equation 23

From Equation 18 the individual heat components will be isolated for possible quantification in the following tests.

Test 1

The first test quantifies the ambient heat component by not adding gaseous oxygen, gaseous helium, or liquid nitrogen through the heat exchanger. This type of operation is typically termed normal evaporation, and the mass flow rate exiting the IRAS is typically termed the Normal Evaporation Rate. Under the normal evaporation configuration,

Equation 18 reduces to Equation 24.

$$Q_{\dot{m}_{GO_2}} = Q_{\dot{m}_{GHe}} = Q_{HX} = 0$$

$$Q_{AMB} = Q_{EVAP}$$

Equation 24

Test 2

The second test quantifies the efficiency the heat exchanger by operating the IRAS dewar in a zero boil-off (ZBO) configuration, or no evaporation, while neither gaseous oxygen nor gaseous helium enter the IRAS dewar. Three variations of Test 2 are run, which varies the vertical height of the IRAS heat exchanger. Under ZBO conditions,

Equation 18 reduces to Equation 25.

$$Q_{\dot{m}_{GO_2}} = Q_{\dot{m}_{GHe}} = Q_{EVAP} = 0$$

$$Q_{AMB} = Q_{HX}$$

Equation 25

Test 3

The third test quantifies the liquefaction rate of the IRAS dewar. Gaseous oxygen enters the IRAS dewar, while the IRAS maintains ZBO conditions and no gaseous helium enters the IRAS dewar. Two variations of Test 3 are run; one test flows gaseous oxygen into the ullage, while the other test flows gaseous oxygen into the liquid. The two tests are intended to isolate the condensation rate, or liquefaction rate, at the surface of the liquid. For the liquefaction runs, Equation 18 reduces to Equation 26.

$$Q_{\dot{m}_{GHe}} = Q_{EVAP} = 0$$

$$Q_{AMB} + Q_{\dot{m}_{GO_2}} = Q_{HX}$$

Equation 26

Test 4

The fourth test quantifies the densification rate of liquid oxygen in the IRAS dewar. Since the ullage pressure becomes sub-atmospheric if the temperature of liquid oxygen is reduced below its normal boiling point, gaseous helium enters the IRAS dewar in order to maintain a positive pressure. Under the densification conditions, IRAS still maintains ZBO conditions and no gaseous oxygen flows into the IRAS. Under densification conditions,

Equation 18 reduces to Equation 27.

$$Q_{\dot{m}_{GO_2}} = Q_{EVAP} = 0$$

$$Q_{AMB} + Q_{\dot{m}_{GHe}} = Q_{HX}$$

Equation 27

Test Matrices

As noted in Chapter Two, Test 1 has already been performed and the ambient heat input reported as 17.5W. The remaining tests will be performed at three different IRAS dewar pressures. Table 4 and Table 5 show the test matrices to accomplish Test 2 and Test 3.

Table 4: Test 2 Matrix – Zero Boil-off

Test Run Number	IRAS Set Pressure	Gaseous Oxygen Flow Rate	
		Percentage of Maximum	Oxygen Flow Rate
Test Run 2a	3 psig (20.7 kPag)	0% Max. GO_2	0 sLm
Test Run 2b	5 psig (34.5 kPag)	0% Max. GO_2	0 sLm
Test Run 2c	7 psig (48.3 kPag)	0% Max. GO_2	0 sLm

Table 5: Test 3 Matrix – Liquefaction

Test Run Number GO_2 Top Fill	Test Run Number GO_2 Bottom Fill	IRAS Set Pressure	Gaseous Oxygen Flow Rate	
			Percentage of Maximum	Oxygen Flow Rate
Test Run 3a	Test Run 3m	3 psig (20.7 kPag)	25% Max. GO_2	2.5 sLm
Test Run 3b	Test Run 3n		50% Max. GO_2	sLm
Test Run 3c	Test Run 3o		75% Max. GO_2	sLm
Test Run 3d	Test Run 3p		100% Max. GO_2	sLm
Test Run 3e	Test Run 3q	5 psig (34.5 kPag)	25% Max. GO_2	sLm
Test Run 3f	Test Run 3r		50% Max. GO_2	sLm
Test Run 3g	Test Run 3s		75% Max. GO_2	sLm
Test Run 3h	Test Run 3t		100% Max. GO_2	sLm
Test Run 3i	Test Run 3u	7 psig (48.3 kPag)	25% Max. GO_2	sLm
Test Run 3j	Test Run 3v		50% Max. GO_2	sLm
Test Run 3k	Test Run 3w		75% Max. GO_2	sLm
Test Run 3l	Test Run 3x		100% Max. GO_2	sLm

Table 6 shows the densification test matrix. Test Runs 4a – 4d are the densification runs that allow the IRAS dewar to operate at a pressure lower than atmospheric pressure. Sub-atmospheric operation occurs because the condensable ullage, gaseous oxygen, remains above the liquid throughout the densification test run. Test Runs 4e – 4p are the densification runs that operate the IRAS at pressures above atmospheric by replacing the gaseous oxygen that condenses with non-condensable gaseous helium.

Table 6: Test 4 Matrix – Densification

Test Run Number	IRAS Set Pressure	Gaseous Nitrogen Flow Rate		Ullage Gas
		Percentage of Available	Nitrogen Flow Rate	
Test Run 4a	Subatmospheric <0 psig (<0 kPag)	25% GN_2 Avail.	40 sLm	GO_2
Test Run 4b		50% GN_2 Avail.	60 sLm	GO_2
Test Run 4c		75% GN_2 Avail.	80 sLm	GO_2
Test Run 4d		100% GN_2 Avail.	100 sLm	GO_2
Test Run 4e	3 psig (20.7 kPag)	25% GN_2 Avail.	40 sLm	GHe
Test Run 4f		50% GN_2 Avail.	60 sLm	GHe
Test Run 4g		75% GN_2 Avail.	80 sLm	GHe
Test Run 4h		100% GN_2 Avail.	100 sLm	GHe
Test Run 4i	5 psig (34.5 kPag)	25% GN_2 Avail.	40 sLm	GHe
Test Run 4j		50% GN_2 Avail.	60 sLm	GHe
Test Run 4k		75% GN_2 Avail.	80 sLm	GHe
Test Run 4l		100% GN_2 Avail.	100 sLm	GHe
Test Run 4m	7 psig (48.3 kPag)	25% GN_2 Avail.	40 sLm	GHe
Test Run 4n		50% GN_2 Avail.	60 sLm	GHe
Test Run 4o		75% GN_2 Avail.	80 sLm	GHe
Test Run 4p		100% GN_2 Avail.	100 sLm	GHe

CHAPTER FOUR: RESULTS AND DISCUSSION

Initial IRAS Checkout

Instrument Checkout

Prior to liquid oxygen test runs, the IRAS was filled with liquid nitrogen to checkout or ensure proper performance of the pressure, temperature, and flow instrumentation. Initially, the IRAS was subjected to atmospheric pressure by opening of hand valve, HV-2. During this phase of checkout, resistance temperature diode, T27, T30, T32,and T33 read off-scale high at 1123K, while thermocouple, TC1 read off-scale high at 2048K. These temperature sensors were not replaced because T26 measures the temperature of a lateral position provides no relevant information for the calculations of liquefaction and densification. The T31 thermocouple was damaged during the installation of the teflon tubing on the vent and fill tubing in the IRAS heat exchanger. The T31 thermocouple was intended to measure the temperature of the IRAS heat exchanger exit, however, previous tests show the location of the thermocouple did not measure the nitrogen at the heat exchanger exit well.

The second phase of checkout ensured the proper performance of the pressure transducers. The pressure transducers were calibrated by the NASA-KSC calibration laboratory and found to have an error of . The IRAS dewar was allowed to pressurize to the relief valve, RV-11, set at 8 psig. The pressure gauge, PG-6, correlated well with the PT-7 as read on the Labview program during the pressurization. The IRAS heat exchanger loop was pressurized with helium to 25 psig, as recorded with a separate pressure gauge.

IRAS Heat Exchanger Leak Check

As mentioned in Chapter Three, stainless steel and copper compose the IRAS heat exchanger. The tubing were connected using a threaded fitting at ambient conditions and as the metals cool to liquid nitrogen temperatures, the two metals contract at different rates. A pressure decay test was conducted to ensure the IRAS heat exchanger did not develop a leak during cool down. While liquid nitrogen was in the IRAS dewar, the IRAS heat exchanger loop was pressurized to approximately 25 psig with gaseous helium and allowed to decay for fifteen minutes. The pressure decay was approximately 0.5 psig over the fifteen minutes and the profile is shown in Figure 7. Equation 28 represents an isentropic pressure vessel blowdown analysis, while Equation 29 represents an isothermal blowdown analysis to estimate the size of the leak within the heat exchanger loop [28]. Equation 28 and Equation 29 estimate a 0.00013 inch diameter leak and 0.00016 inch diameter leak, respectively. Equation 30 estimates the mass flow rate [29] through the leak at 0 0.0081 sLm of nitrogen and 0.0081 sLm of nitrogen by the isentropic blowdown analysis and isothermal blowdown analysis, respectively.

$$\frac{\mathrm{P}}{\mathrm{P_i}} = \left[1 + \left(\frac{\gamma - 1}{2}\right)\left(\frac{2}{\gamma + 1}\right)^{\frac{(\gamma+1)}{2(\gamma-1)}} \sqrt{\frac{\gamma\, g_c \mathrm{P_i}}{\rho_i}}\ \frac{\mathrm{A\,t}}{\mathrm{V}}\right]^{\frac{-2\gamma}{(\gamma-1)}}$$

Equation 28

$$\frac{\mathrm{P}}{\mathrm{P_i}} = \exp\left[-\left(\frac{\gamma - 1}{2}\right)\left(\frac{2}{\gamma + 1}\right)^{\frac{(\gamma+1)}{2(\gamma-1)}} \sqrt{\frac{\gamma\, g_c \mathrm{P_i}}{\rho_i}}\ \frac{\mathrm{A\,t}}{\mathrm{V}}\right]$$

Equation 29

$$\dot{m} = \rho\, Q = \rho\, C_D\, A \sqrt{2 \frac{\Delta P\, g_c}{\rho}} = C_D\, A \sqrt{2\, P\, \rho\, g_c}$$

Equation 30

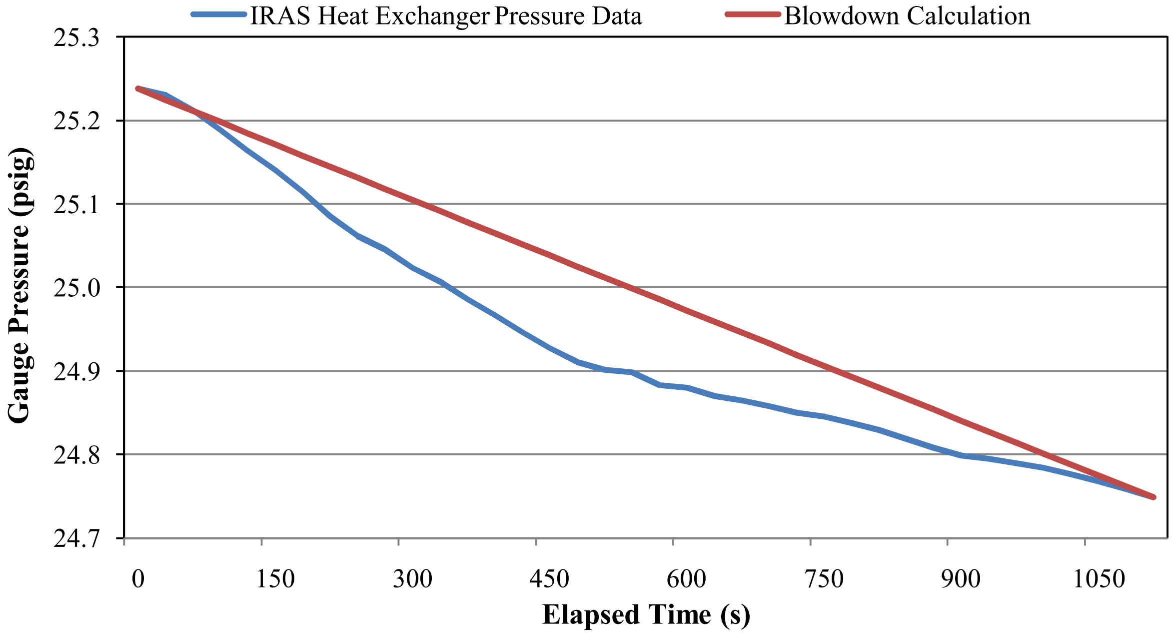

Figure 7: IRAS Heat Exchanger Leak Check

Temperature Profile within the IRAS Dewar

As shown in Figure 8, the temperature profile within the liquid is steady at the boiling point of the liquid. Natural convection currents within the liquid provide sufficient mixing to maintain a uniform temperature with no thermal stratification within the liquid. However, a temperature gradient exists within the ullage and is thermally stratified. Thermal stratification in the ullage occurs because a constant temperature boundary condition exists at the liquid portion of the liquid-vapor interface due to the consequent vaporization. Heat transfer from the ambient warms the vapor at the dewar wall causing the vapor to become less dense and more buoyant. Because the lowest temperature in the ullage exists at the bottom of the ullage, natural convection is too weak to provide sufficient mixing within the ullage.

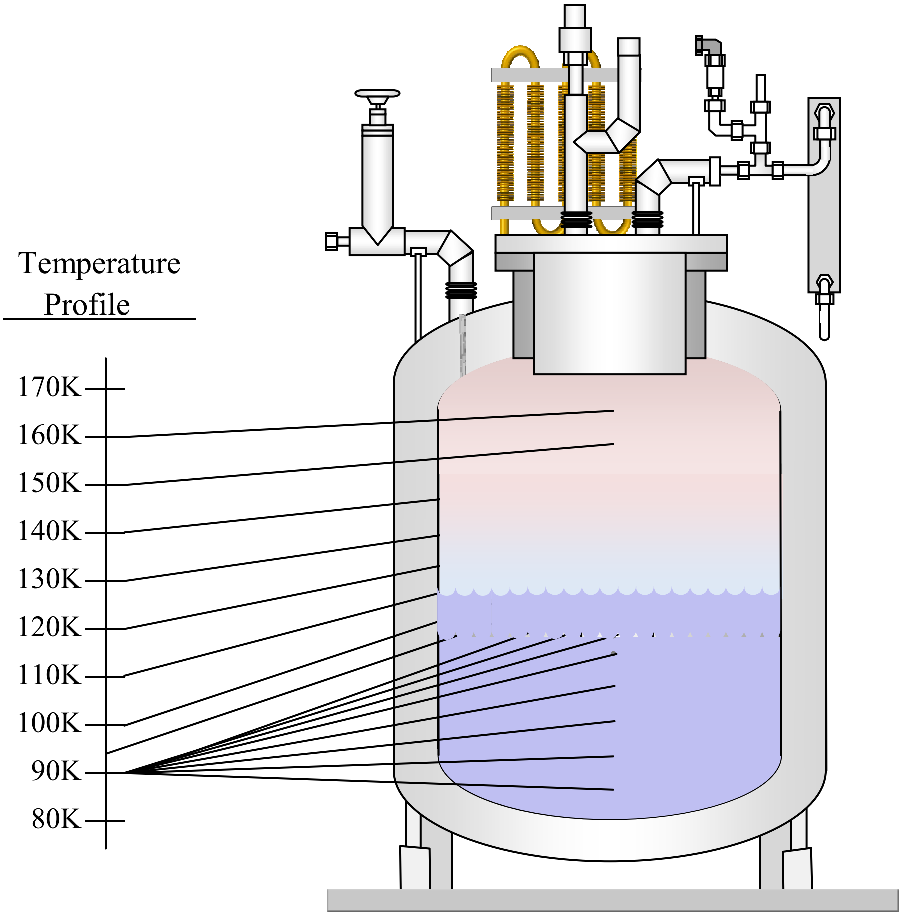

Figure 8: Temperature Profile of IRAS Containing Liquid Oxygen

Normal Evaporation Test

From Equation 24, the heat transferred to the IRAS dewar from the ambient can be determined by measuring the mass flow rate that evaporates from IRAS. The heat released from the IRAS with the evaporation is calculated by Equation 31.

$$Q_{EVAP} = \dot{m}(h_f - h_i) = \dot{m}\left[\int_{T_i}^{T_{BP}} c_{P,L} dT + h_{LV} + \int_{T_{BP}}^{T_f} c_{P,V} dT\right]$$

Equation 31

Once the liquid within the IRAS dewar reaches steady conditions, the liquid is saturated at the IRAS dewar pressure, however, a temperature gradient exists within the ullage. Thus, the liquid sensible heat portion of Equation 31 can be neglected, while the vapor sensible heat portion of Equation 31 remains a significant fraction of the total evaporation heat calculation.

As the IRAS dewar was filled with liquid nitrogen, a flow meter was placed on the IRAS dewar vent, downstream of HV-2, during normal venting to measure the mass flow rate of the normal evaporation. The average flow rate over the period of an hour measured 5.3 sLm, and the measured ullage temperature gradient ranges from 77 K to 160 K. The measured flow rate represented an average heat transfer rate of 17.6 W, which agrees well with the value reported by Notardonato.

Zero Boil-off

From Equation 25, the heat transferred to the IRAS dewar from the ambient can be removed by the coolant through the IRAS heat exchanger. The heat removed from the IRAS dewar is measured and calculated by Equation 32.

$$Q_{HX} = \dot{m}_{N_2}\left(h_{HX\,Exit} - h_{HX\,Inlet}\right) = \dot{m}_{N_2}\left[\int_{T_{HX\,Inlet}}^{T_{BP}} c_{P,L}\,dT + h_{LV} + \int_{T_{BP}}^{T_{HX\,Exit}} c_{P,V}\,dT\right]$$

Equation 32

The inlet condition is measured by TC-24 and PT-25 to determine saturation conditions and level of subcooling, while the exit condition is by TC. The cooling requirement as determined by Equation 32 is 21.44W, 21.78W, and 20.32W for IRAS pressures of 3 psig, 5 psig, and 7 psig, respectively.

Liquefaction

From Equation 26, the heat that enters the IRAS dewar with the oxygen flow rate is removed by the coolant through the IRAS heat exchanger. The heat removed from the IRAS dewar is measured and calculated by Equation 26 and Equation 32. Another way to measure the heat removed from the IRAS dewar during the liquefaction tests is by Equation 33.

$$Q_{\dot{m}_{O_2}} = \dot{m}_{O_2}\left(h_{Liquid,BP} - h_{Vapor,Ambient}\right) = \dot{m}_{O_2}\left[h_{LV} + \int_{T_{BP}}^{T_{Ambient}} c_{P,V}dT\right]$$

Equation 33

Equation 26 coupled with Equation 32 or Equation 33 provides the heat transfer for the entire IRAS dewar. Equation 1, Equation 2, Equation 3, Equation 6, and Equation 7 predict the heat and mass transfer at the vapor-liquid interface.

Liquefaction – Top Fill

For the Test Run 3a through Test Run 3l, the gaseous oxygen flows through the IRAS vent valve, HV-2, and enters the IRAS dewar from the top. The gaseous oxygen enters the IRAS dewar at a temperature close to ambient, which is the temperature the gaseous oxygen k-bottle. The gaseous oxygen stream enters as a jet into the ullage, however, the gas begins to rise due to buoyancy effects as soon as the downward velocity dissipates. Figure 9 shows the warm gaseous oxygen entering the IRAS dewar, with the isotherms within the ullage.

Because of the buoyancy effects within the ullage, liquefaction by the top fill method condenses the cold isothermal layers nearest the liquid-vapor interface. No mass motion occurs in the ullage except for the general bulk downward movement of the ullage to replace the volume occupied by the vapor that is condensed. Thus, the heat transfer from the liquid surface to the gaseous oxygen is conduction dominant. Nevertheless, heat is transferred within the liquid oxygen by natural convection currents.

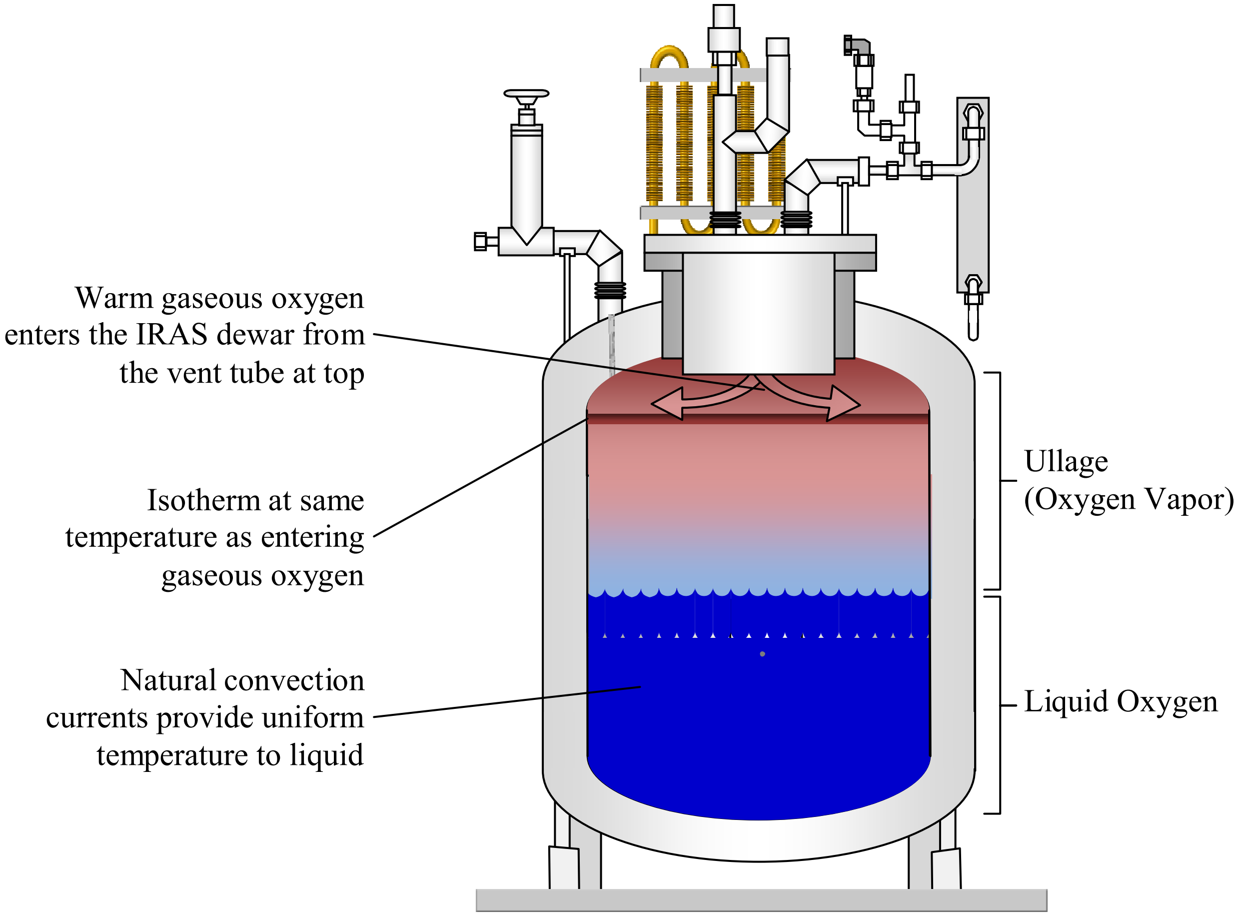

Figure 9: Convection Currents within IRAS Dewar during Top Fill Liquefaction

Figure 10 shows the results of the cooling requirement for Test Run 3a through Test Run 3l. The cooling requirement was calculated by Equation 32, where TC-22 and PT-25 provide the nitrogen inlet conditions and TC provide the exit conditions. The cooling requirement for gaseous oxygen condensation rate decreases with increasing pressures within the IRAS dewar, as measured by PT-7. Condensation of oxygen at varying pressures requires different cooling requirements because of (1) oxygen latent heat decreases as pressure increases, and (2) sensible heat decreases as pressure increases due to the higher boiling point. However, the increase in measured cooling requirement with respect to IRAS dewar pressure is much greater than the calculated cooling requirement to condense oxygen at the higher pressures. The cooling requirement increases as the oxygen condensation rate increases; the measured cooling requirement, as shown in Figure 10, agrees with calculated cooling requirement increase of approximately 8W/sLm.

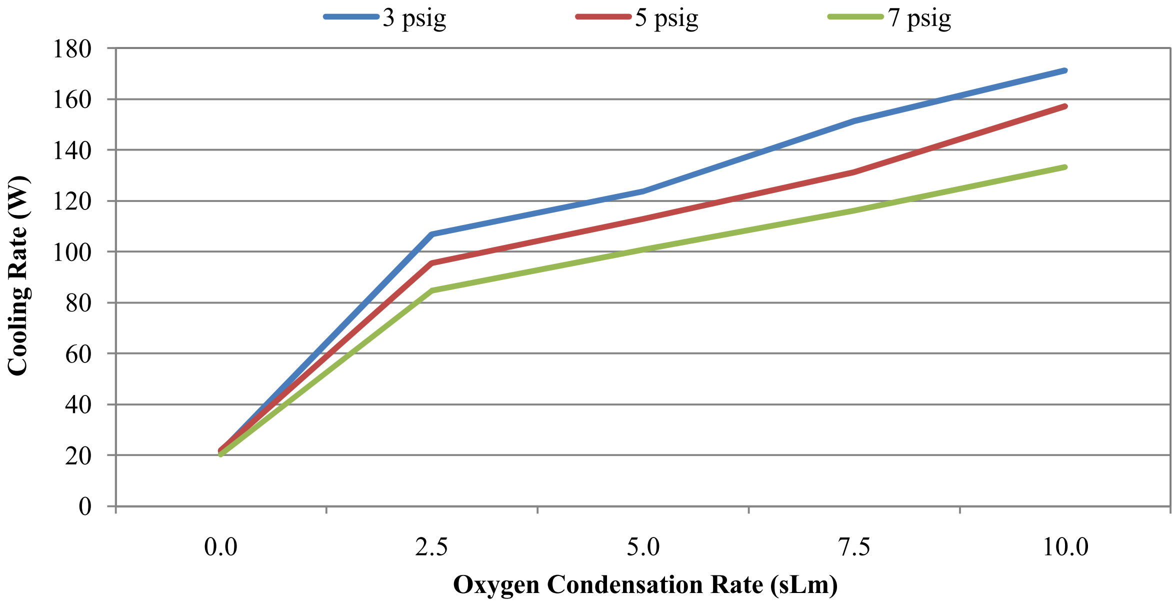

Figure 10: Cooling Rate at Constant Oxygen Flow Rate and Pressure

Using temperature and pressure measurements during the test runs 3a through 3l, Equation 1, Equation 3, and Equation 6 estimate the oxygen condensation rate through direct contact. Figure 11, Figure 12, and Figure 13 show the results of the estimates provided by Equation 1, Equation 3, and Equation 6, respectively. The results of Equation 1 and Equation 3 are six orders of magnitude larger than the actual oxygen condensation rate, while the results of Equation 6 are an order of magnitude smaller than the actual oxygen condensation rate.

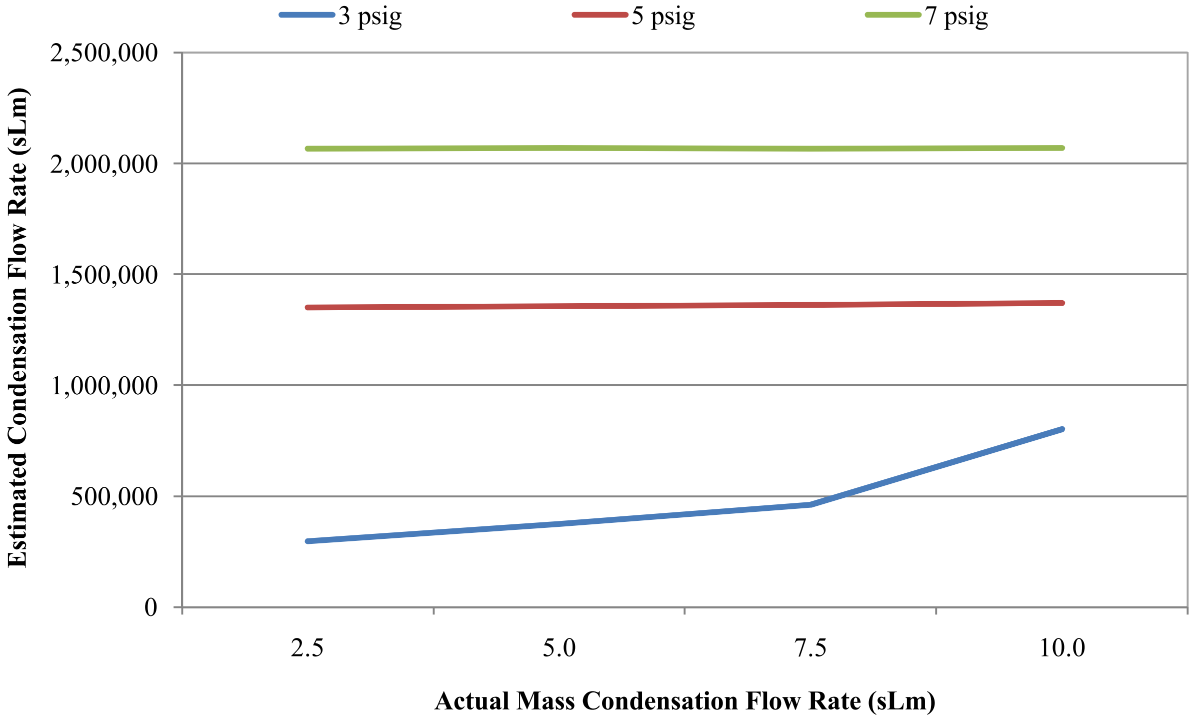

Figure 11: Equation 1 Results for Test Run 3a through Test Run 3l

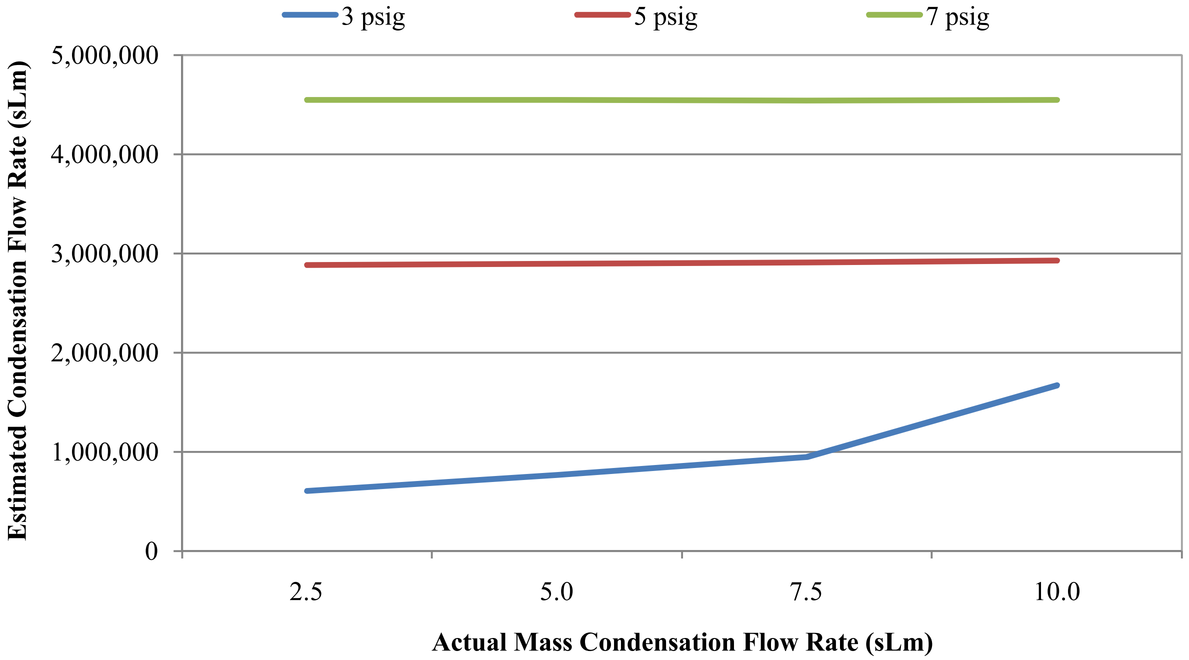

Figure 12: Equation 3 Results for Test Run 3a through Test Run 3l

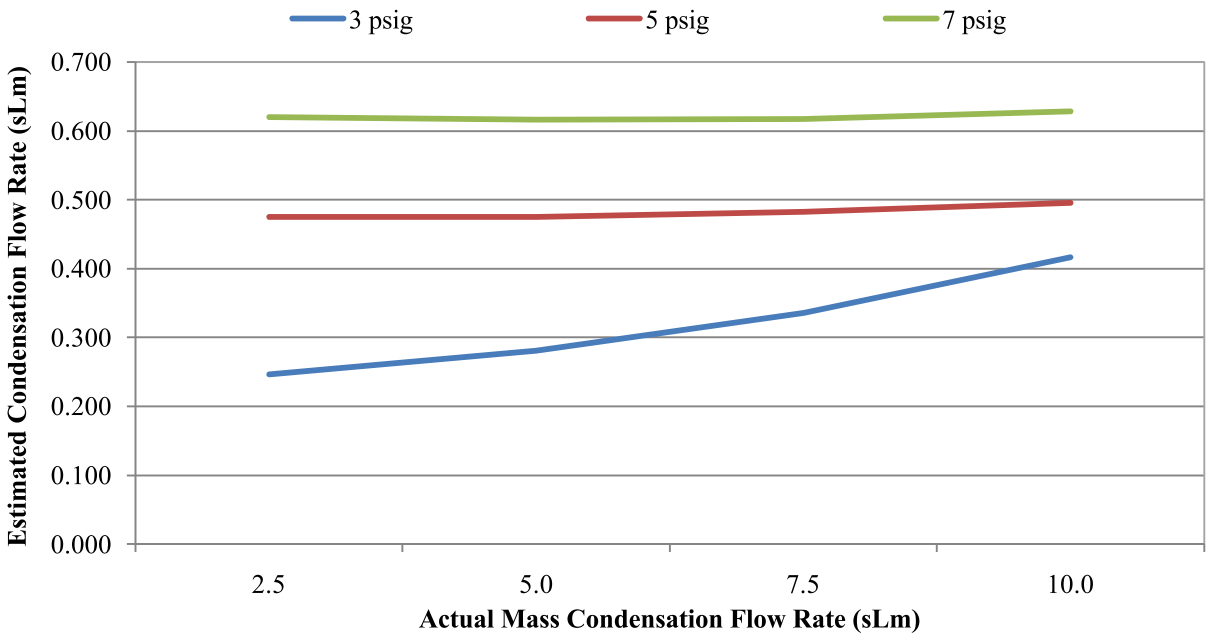

Figure 13: Equation 6 Results for Test Run 3a through Test Run 3l

The two kinetic theory models (Equation 1 and Equation 3) depend on the temperature at the vapor-liquid interface. However, the temperature sensor on each side of the vapor-liquid interface are separated by a distance of four inches and a minimum temperature difference of 3K.

Liquefaction – Bottom Fill

For Test Run 3m through Test Run 3x, the gaseous oxygen enters the IRAS dewar through the hand valve, HV-1, to the liquid oxygen fill line. The liquid oxygen fill line is routed through the annular space and enters the inner tank near the top and runs vertically down the interior of the tank to the bottom as shown in Figure 14. The gaseous oxygen temperature is close to ambient as it enters the liquid oxygen fill line, however, the gaseous oxygen cools while flowing down the liquid oxygen fill line. The gaseous oxygen departs the liquid oxygen fill line as bubbles that flows upward through the liquid oxygen and into the ullage.

The gaseous oxygen within the bubbles continue to cool and collapse as the bubbles rise through the liquid oxygen. If insufficient cooling is provided to the bubble, the gaseous oxygen eventually reaches the liquid oxygen surface. The gaseous oxygen continues to rise into the ullage until the it reaches the isotherm equal to the temperature of the cooled gaseous oxygen as shown in Figure 14. The bottom fill takes advantage of the convection currents within the liquid to provide cooling to the gaseous oxygen bubble as well as placing the gaseous oxygen in the ullage at a distance closer to the liquid surface. Since the ullage remains conduction dominant, the shorter distance to the liquid surface allows for more efficient heat transfer than the top fill where the gaseous oxygen is placed at the top of the IRAS dewar.

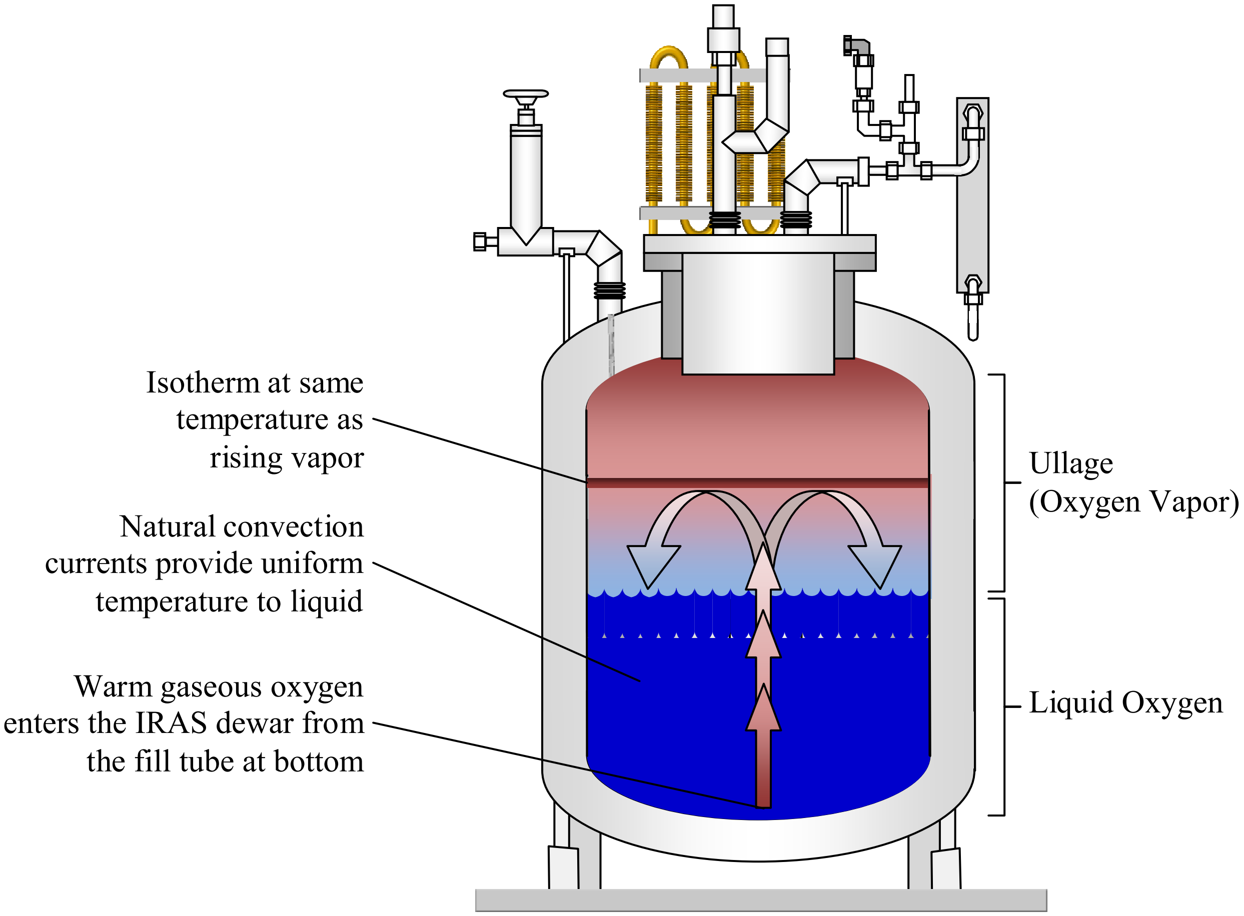

Figure 14: Convection Currents within IRAS Dewar during Bottom Fill Liquefaction

Densification

Helium solubility in liquid oxygen is in the 17 ppm, 28 ppm, and 40 ppm for pressure of 3 psig, 5 psig, and 7 psig from calculations from Zimmerli et. al. [29].

APPENDIX A: HEAT TRANSFER ANALYSIS

Heat Transfer Analysis Through Teflon Insulation

The vertical tubing carrying the liquid nitrogen to the heat exchanger and the vaporized gaseous nitrogen from the heat exchanger needs to be insulated to minimize heat transfer into the ullage. It is desired to optimize the insulation thickness before specifying the design requirements for the insulation. An optimum insulation thickness, or heat transfer minimum, does not exist for radial systems, but a heat transfer maximum can exist [18]. To ensure that the insulation thickness inhibits heat transfer, the heat transfer through the fill and vent tubes are analyzed.

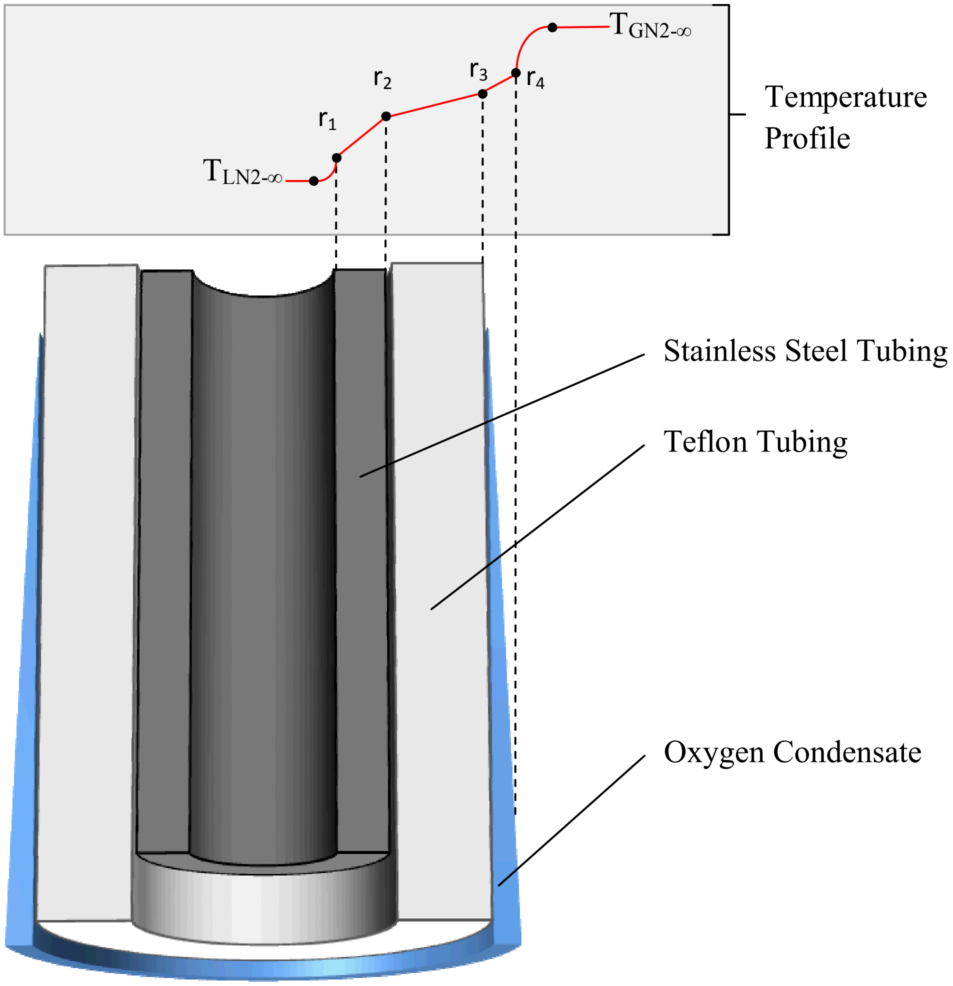

Figure 15: Fill and Vent Tubing Thermal Resistance Model

Figure 15 shows cutaway of the fill and vent tubes. The fill and vent tubes are composed of the stainless steel tubing surrounded by the Teflon tubing as insulation. Depending on the Teflon outer wall temperature, oxygen may condense on the outside of the Teflon. The nitrogen flows down through the fill tube as two phase fluid; then the nitrogen flows up through the vent tube as a gas. The outside of both the fill and vent tube is the natural convection. Heat transfers from the gaseous oxygen ullage through the natural convection boundary layer, through the oxygen condensate, through the Teflon and stainless steel by conduction, and through the internal convection layer.

Overall Radial Heat Transfer to the Fill Tube and Vent Tube – Incropera (3.29 & 3.30)

Equation 34 calculates the overall heat transfer through the fill and vent tubes [18].

$$q_r = \frac{T_{GO_2-\infty} - T_{LN_2-\infty}}{R_{tot}}$$

Equation 34

$$q_r = \frac{T_{GO_2-\infty} - T_{LN_2-\infty}}{\frac{1}{2\pi r_1 L h_{IC}} + \frac{\ln\left(\frac{r_2}{r_1}\right)}{2\pi k_{SS} L} + \frac{\ln\left(\frac{r_3}{r_2}\right)}{2\pi k_{PTFE} L} + \frac{1}{2\pi r_3 L h_{CC}} + \frac{1}{2\pi r_4 L h_{EC}}}$$

Equation 35

Convection of Nitrogen Flowing Inside Fill Tube

Equation 36 through Equation 44 develop the convective heat transfer coefficient from the stainless steel tube wall to the nitrogen. Even though the nitrogen is precooled before entering the IRAS, these calculations assume two-phase flow once entering the fill tube. Two correlations were used to evaluate the heat transfer coefficient, the Chen correlation and the Kandlikar correlation, which provided the same order of magnitude result. The Chen correlation sums the convective contributions from the bulk convection and the microscopic nucleate boiling [30].

$$h_{IC} = h_{mic} + h_{mac}$$

Equation 36

$$h_{mic} = 0.00122\left[\frac{k_l^{0.79}c_{pl}^{0.45}\rho_l^{0.49}}{\sigma^{0.5}\mu_l^{0.29}h_{lv}^{0.24}\rho_v^{0.24}}\right][T_w - T_{sat}(P_l)]^{0.24}[P_{sat}(T_w) - P_l]^{0.75}S$$

Equation 37

$$S(Re_{tp}) = \left(1 + 2.56x10^{-6}Re_{tp}^{1.17}\right)^{-1}$$

Equation 38

$$Re_{tp} = Re_l[F(X_{tt})]^{1.25}$$

Equation 39

$$X_{tt} = \left(\frac{1-x}{x}\right)^{0.9}\left(\frac{\rho_v}{\rho_l}\right)^{0.5}\left(\frac{\mu_l}{\mu_v}\right)^{0.1}$$

Equation 40

$$F(X_{tt}) = \begin{cases} 1 & X_{tt}^{-1} \leq 0.1 \\ 2.35\left(0.213 + \frac{1}{X_{tt}}\right)^{0.736} & X_{tt}^{-1} < 0.1 \end{cases}$$

Equation 41

$$h_{mac} = h_l F(X_{tt})$$

Equation 42

$$h_l = 0.023\left(\frac{k_l}{D}\right)Re_l^{0.8}Pr_l^{0.4}$$

Equation 43

$$Re_l = \frac{4\dot{m}}{\pi\mu_l D}$$

Equation 44

Convection of Nitrogen Flowing Inside Vent Tube - Incropera (8.55), (8.63), (8.21)

Equation 45 calculates the convective heat transfer coefficient across the boundary layer from forced convection of the gaseous nitrogen flowing upward through the inside of the vent tube. Equation 45 is developed by solving the Navier-Stokes energy equation in cylindrical coordinates and assuming (1) laminar, fully developed flow and (2) isothermal inner vent tube wall[18].

$$h_{IC} = \frac{k_v}{D} Nu_D = 3.66 \frac{k_v}{D}$$

Equation 45

Equation 46 calculates the convective heat transfer coefficient across the boundary layer from forced convection of the gaseous nitrogen flowing upward through the inside of the vent tube [18]. Equation 46 uses the Gnielinski correlation by assuming (1) turbulent flow through (2) a smooth tube. For the most realistic flow regimes (GN_2 flows above 5 sLm), the GN_2 flow is turbulent.

$$h_{IC} = \frac{k_v}{D} Nu_D = \frac{k_v}{D}\left[\frac{(f/8)(Re_D - 1000)Pr}{1 + 12.7(f/8)^{1/2}(Pr^{2/3} - 1)}\right]$$

Equation 46

$$f = (0.790 \ln Re_D - 1.64)^{-2}$$

Equation 47

Condensation Correlation – Incropera (10.30), (10.26), (10.33)&(10.34), (10.38), (10.39)

Equation 48 represents the condensation convection coefficient and was developed using the Nusselt approximation for laminar flow, which is conditional on the value of the Reynolds number defined by Equation 50. Equation 51 and Equation 52 represent the condensation convection coefficient for the wavy and turbulent flow, respectively [18].

$$\bar{h}_{CC} = 0.943\left[\frac{g\rho_l(\rho_l - \rho_v)k_l^3 h_{lv}^{'}}{\mu_l(T_{sat} - T_s)L}\right]$$

Equation 48

$$h_{lv}^{'} = h_{lv}(1 + 0.68Ja)$$

Equation 49

$$Re_\delta = \frac{4\bar{h}_L(T_{sat} - T_s)L}{\mu_l h_{lv}^{'}}$$

Equation 50

$$\frac{\bar{h}_{CC}\left(\nu_l^2/g\right)^{1/3}}{k_l} = \frac{Re_\delta}{1.08Re_\delta^{1.22} - 5.2} \qquad 30 \leq Re_\delta \leq 1800$$

Equation 51

$$\frac{\bar{h}_{CC}\left(\nu_l^2/g\right)^{1/3}}{k_l} = \frac{Re_\delta}{8750 + 58Pr^{-0.5}\left(Re_\delta^{0.75} - 253\right)} \qquad Re_\delta > 1800$$

Equation 52

Natural Convection of Gaseous Oxygen Outside Fill Tube and Vent Tube – Incropera (9.27)

Equation 53 calculates the convective heat transfer coefficient through boundary layer developed by the natural convection[18]. Equation 53 assumes (1) flat, vertical plate analysis and (2) isothermal tube wall temperature and suggested for Rayleigh numbers below 10^9. The flat plate assumption can be applied to vertical cylinders if the boundary layer is much less than diameter of the cylinder; the condition is satisfied by Equation 54. The assumption that the tube walls are isothermal is a great approximation for the fill tube because the nitrogen is saturated and heat transferred to the nitrogen from the ullage gas produces a phase change and not a temperature change, thus, the nitrogen maintains the tube wall temperature. Although heat transferred to the nitrogen in the vent tube produces a temperature increase, the temperature increase is minimal, typically less than 10°C, and the isothermal assumption for the vent tube outer wall remains a good approximation.

$$h_{EC} = \frac{k_{GO_2}}{D}\overline{Nu_D} = \frac{k_{GO_2}}{D}\left[0.68 + \frac{0.670Ra_D^{1/4}}{\left[1+\left(\frac{0.492}{Pr}\right)^{9/16}\right]^{4/9}}\right]$$

Equation 53

$$\frac{D}{L} = \frac{35}{Gr_L^{1/4}}$$

Equation 54

The results for simultaneous solutions for Equation 34 through Equation 53 as a function of insulation thickness are shown in Figure 16 and Figure 17 for the fill tube and vent tube, respectively. Each figure shows a “break-even” insulation thickness, which is the minimal insulation thickness required to make any thermal resistance improvements. The proposed insulation thickness is 1.0625 inches and 1 inch for the fill tube and vent tube, respectively, and is shown by the arrow on the right hand side of the figure pointing upward. The proposed insulation decreases the heat transfer through the fill tube and vent tube by 1.1W and 2.7W, respectively.

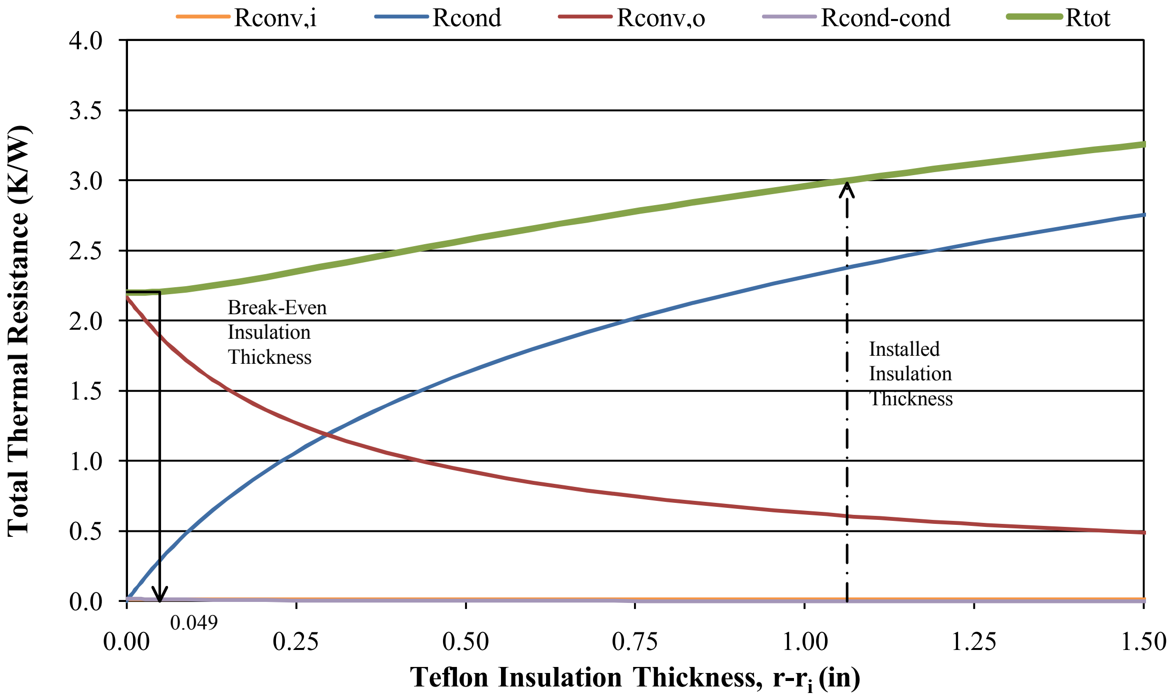

Figure 16: Fill Tube Insulation Optimization

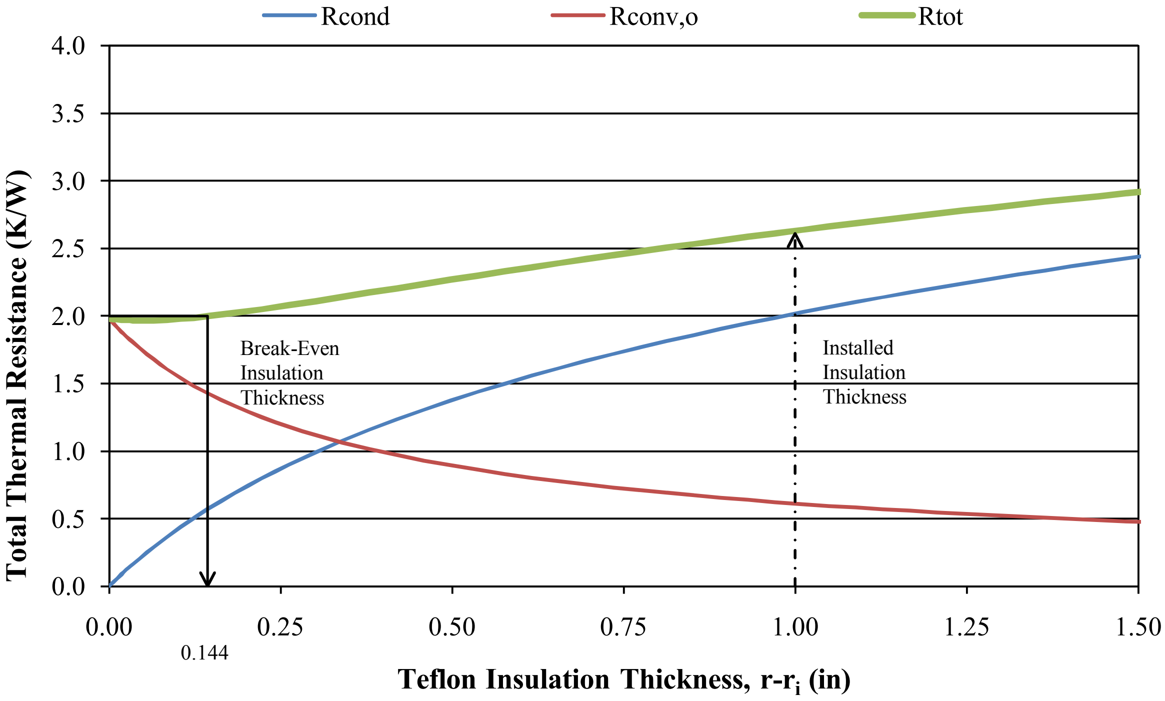

Figure 17: Vent Tube Insulation Optimization

Heat Transfer Analysis for IRAS Heat Exchanger

The IRAS heat exchanger is a ½" copper tubing in the shape of a "U" with annular fins. Figure 18 represents the heat exchanger and Figure 19 represents a cross-section of the IRAS heat exchanger for calculation purposes. The variables in Figure 19 are consistent with fin heat transfer presented in Incropera [18]. The overall length of the heat exchanger is 14 inches and the fins extend 5/16" in the radial direction from the base of the tubing.

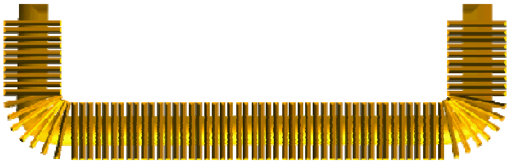

Figure 18: IRAS Heat Exchanger

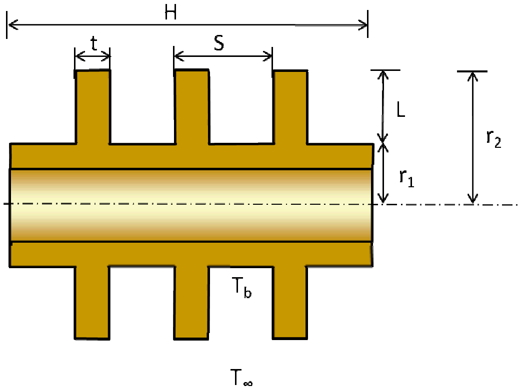

Figure 19: IRAS Heat Exchanger Cross-Section

The heat transfer through the IRAS heat exchanger is calculated from From Incropera (3.101):

$$q_t = h\,A_t\left[1 - \frac{N\,A_f}{A_t}(1 - \eta_f)\right]\theta_b$$

Equation 55

From Incropera (9.33) and (9.34), The convective heat transfer coefficient is given by Equation 56:

$$\overline{Nu}_D = \frac{\bar{h}D}{k} = \left\{0.60 + \frac{0.387Ra_D^{1/6}}{[1 + (0.559/Pr)^{9/16}]^{8/27}}\right\}^2$$

Equation 56

From Incropera (3.99), the total surface area of the heat exchanger is given by Equation 57:

$$A_t = NA_f + A_b = NA_f + 2\pi r_1(H - Nt)$$

Equation 57

From Incropera Table 3.5 for straight fins:

$$A_f = 2\pi\left(r_{2,c} - r_1\right)^2$$

Equation 58

From Incropera (3.89) and (3.90), the single fin efficiency is given by Equation 59:

$$\eta_f = \frac{\tanh mL_c}{mL_c} = \frac{\tanh\left[\left(\frac{2h}{kA_p}\right)^{1/2} L_c^{3/2}\right]}{\left[\left(\frac{2h}{kA_p}\right)^{1/2} L_c^{3/2}\right]}$$

Equation 59

The heat exchanger is capable of transferring 3,400 W of heat. The fins increase the heat transfer rate capability by approximately 1000% when compared to a copper tube without fins.

APPENDIX B: EXPERIMENTAL SETUP INFORMATION

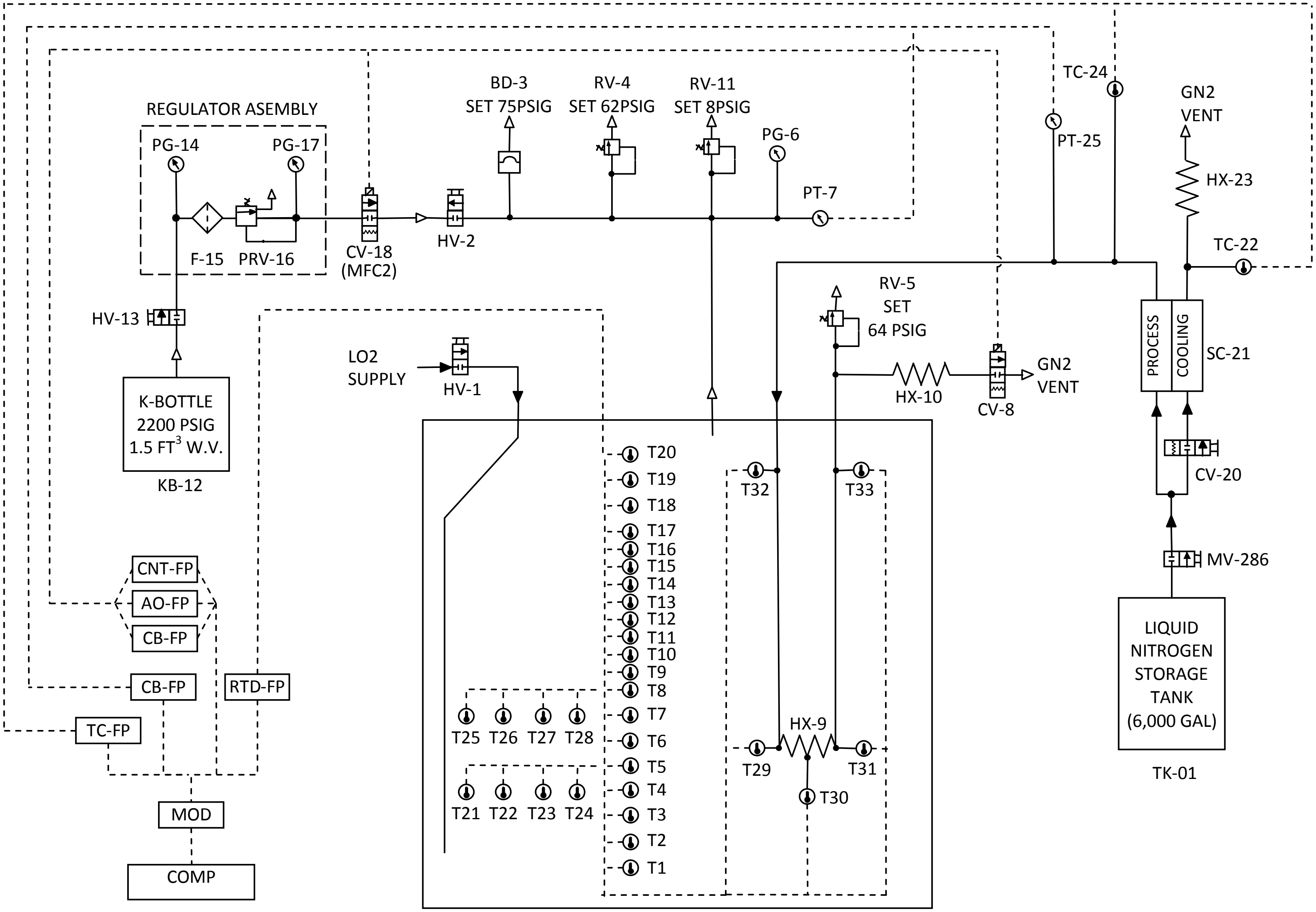

Figure 20: Experimental Setup - Detailed Process Instrumentation Diagram

Table 7: Experimental Setup - Detailed Process Instrumentation Legend

REFERENCE DESIGNATOR	DESCRIPTION	SPECIFICATION	MANUFACTURER	MANUFACTURER NUMBER
TK-01	LIQUID NITROGEN TANK	6,000 GALLON	MINNESOTA VALLEY	VCS-6000-SC-250
HV-1	IRAS DEWAR INLET VALVE (TYPICALLY LO2)	½”	EDEN CRYOGENICS	BC-02042-8101-1
HV-2	IRAS DEWAR EXIT VALVE (GO2 VENT)	½”	EDEN CRYOGENICS	BC-02042-8100-1
BD-3	IRAS BURST DISC	75PSIG	FIKE CORPORATION	P ST
RV-4	IRAS MAIN RELIEF VALVE	SET 61.7PSIG, 84SCFM	FLOWSAFE, INC	01-2190M-101
RV-5	IRAS COOLANT LOOP RELIEF VALVE	SET 63PSIG	FLOWSAFE, INC.	01-2190M-101
PG-6	IRAS DEWAR PRESSURE GAUGE	0-100 PSIG	ASHCROFT	1008
PT-7	IRAS DEWAR PRESSURE TRANSDUCER	0-25PSIG	TELEDYNE TABER	2415
CV-8	IRAS COOLANT LOOP MASS FLOW CONTROL VALVE	0-100 SLM ± 1SLM	TELEDYNE INSTR.	HFC-203
HX-9	IRAS HEAT EXCHANGER	½” COPPER TUBE		
HX-10	IRAS COOLANT LOOP AMBIENT HEAT EXCHANGER	½” COPPER TUBE		
RV-11	IRAS OPERATIONAL RELIEF VALVE	SET 8PSIG		
KB-12	GASEOUS OXYGEN/HELIUM K-BOTTLE	1.5 FT³ (W.V)		
HV-13	K-BOTTLE ISOLATION VALVE			
PG-14	K-BOTTLE UPSTREAM PRESSURE GAUGE	0-4000 PSI	CONCOA	312-4311-540
F-15	GASEOUS OXYGEN FILTER	10 MICRON		
PRV-16	K-BOTTLE PRESSURE REGULATING VALVE	3000PSI TO 0-250PSI		
PG-17	K-BOTTLE DOWNSTREAM PRESSURE GAUGE	0-400 PSI		
CV-18	GASEOUS OXYGEN MASS FLOW CONTROL VALVE	0-20 SLM ± 0.2SLM	MKS INSTRUMENTS	1179A
MV-286	LIQUID NITROGEN STORAGE TANK ISOLATION VALVE		PHPK	
CV-20	SUBCOOLER CONTROL VALVE			970272-5300-21
SC-21	SUBCOOLER			
TC-22	SUBCOOLER COOLING FLUID EXIT THERMOCOUPLE	TYPE T (-200 to 350°C)	OMEGA	
HX-23	SUBCOOLER COOLING FLUID AMBIENT HEAT EXCHANGER			
TC-24	SUBCOOLER PROCESS FLUID EXIT THERMOCOUPLE	TYPE T (-200 to 350°C)	OMEGA	
PT-25	SUBCOOLER PROCESS FLUID EXIT PRESSURE TRANSDUCER	0-30 PSIG	WIKA INSTR.	4258112
T1 – T32	IRAS DEWAR POSITION TEMPERATURE SENSOR			

Table 7: Experimental Setup - Detailed Process Instrumentation Legend (Continued)

REFERENCE DESIGNATOR	DESCRIPTION	SPECIFICATION	MANUFACTURER	MANUFACTURER NUMBER
TC-FP	THERMOCOUPLE FIELD POINT	8 CHANNEL	NATIONAL INSTRUM	cFP-TC-120
CB-FP	INTEGRATED CONTROL BLOCK FIELD POINT	8 CHANNEL	NATIONAL INSTRUM	cFP-CB-1
RTD-FP	TEMPERATURE MODULE FIELD POINT	8 CHANNEL	NATIONAL INSTRUM	cFP-RTD-124
AO-FP	ANALOG VOLTAGE OUTPUT MODULE FIELD POINT	8 CHANNEL 0-10V	NATIONAL INSTRUM	cFP-AO-210
CNT-FP	INTELLEGIENT CONTROLLER FIELD POINT	2 PORT	NATIONAL INSTRUM	cFP-2110
MOD	ETHERNET SWITCH MODEM	5 PORT	B&B ELECTRONICS	ELINX EIR205
COMP	COMPUTER	2.99GHz, 1.00GBRAM	DELL	PRECISION 670

APPENDIX C: FLUID COMPOSITION

Nitrogen

NASA procures nitrogen in accordance with the military specification, MIL-PRF-27401. The purity and impurity limits are listed in Table 8 under the column titled, "Procurement Specification." The military specification requires the vendor to verify that the individual tanker load met the procurement specification prior to shipment, and shows an actual concentrations of the liquid procured. In addition to the vendor analysis, NASA randomly samples a tanker and analyzes the sample on a periodic basis. Table 8 provides average results from vendor and NASA analysis.

Table 8: Nitrogen Procurement Specification and Laboratory Analysis

Component	Procurement Specification	Vendor Laboratory Analysis	NASA Laboratory Analysis
Nitrogen	99.5% (min)		>99.99 %
Oxygen	50 ppm (max)		<2 ppm
Total Hydrocarbons	25 ppm (max)		<1 ppm
Water	11.6 ppm (max)		<2 ppm
Argon	Not Required	Not Required	7 ppm

Nitrogen is procured to military specification, MIL-PRF-27401F Grade B.
The unit, ppm, is parts per million by volume as a gas at standard conditions.
A less than ("<") represents a value below the lower detection limit of the analytical equipment.

Oxygen

NASA procures oxygen in accordance with the military specification, MIL-PRF-25508. Table 9 lists the purity and impurity requirements from the military specification. Like the nitrogen, a vendor analysis exist for every oxygen delivery. Unlike the nitrogen, a NASA analysis exists for every oxygen delivery as well. Table 9 shows the average analysis for oxygen.

Table 9: Oxygen Procurement Specification and Laboratory Analysis

Component	Procurement Specification	Vendor Laboratory Analysis	NASA Laboratory Analysis
Oxygen	99.99% (min)	>99.99 %	>99.989 %
Total Hydrocarbons	20 ppm (max)	<10.00 ppm	6 ppm
Water	3 ppm (max)	<3.00 ppm	<2 ppm
Methane	16 ppm (max)	5.53 ppm	6 ppm
Ethane	2 ppm (max)	Not Measured	Not Measured
Propane	1 ppm (max)	<1.00 ppm	Not Measured
Nitrous Oxide	1 ppm (max)	<1.00 ppm	<1 ppm
Halogenated Hydrocarbons	1 ppm (max)	<1.00 ppm	<1 ppm
Carbon Monoxide	1 ppm(max)	<1.00 ppm	<1 ppm
Carbon Dioxide			
Nitrogen	75 ppm(max)	4.50 ppm	<5 ppm
Argon		31.56 ppm	19 ppm
Krypton		Not Measured	<5 ppm
Helium	Not Required	Not Required	<10 ppm

Oxygen is procured to military specification, MIL-PRF-25508G Grade F.
The unit, ppm, is parts per million by volume as a gas at standard conditions.
A less than ("<") represents a value below the lower detection limit of the analytical equipment.

Helium

NASA procures helium in accordance with the military specification, MIL-PRF-27407 as a liquid. The purity and impurity limits are listed in Table 10 under the column titled, "Procurement Specification." The military specification requires the vendor to verify that the individual tanker load met the procurement specification prior to shipment, and shows an actual concentrations of the liquid procured. In addition to the vendor analysis, NASA randomly samples a tanker and analyzes the sample on a periodic basis. Table 10 provides average results from vendor and NASA analysis.

Table 10: Helium Procurement Specification and Laboratory Analysis

Component	Procurement Specification	Vendor Laboratory Analysis	NASA Laboratory Analysis
Helium	99.95% (min)		
Water	9 ppm (max)		
Total Hydrocarbons	5 ppm (max)		
Oxygen	3 ppm (max)		
Nitrogen + Argon	14 ppm (max)		
Neon	23 ppm (max)		
Hydrogen	1 ppm (max)		
Carbon Dioxide	1 ppm (max)		
Carbon Monoxide	1 ppm (max)		

Helium is procured to military specification, MIL-PRF-27407C Grade A.
The unit, ppm, is parts per million by volume as a gas at standard conditions.

APPENDIX D: HEAT TRANSFER COEFFICIENT DERIVATION

Direct Contact Condensation by Vapor Collapse

Consider a flat, horizontal, cold plate with quiescent saturated oxygen vapor above the cold plate. A film of liquid oxygen condenses on the cold plate, with the film thickness, δ(t), increasing with time as shown in Figure 21. A control volume, represented by the dotted line, is established around the liquid-vapor interface. The energy balance through the control volume is given by Equation 60.

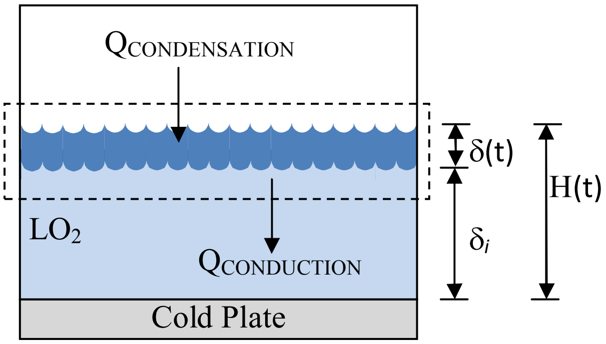

Figure 21: Heat Transfer Coefficient Derivation Model

$$\mathrm{Q_{CONDENSATION}} = \mathrm{Q_{CONDUCTION}}$$

Equation 60

$$\dot{\mathrm{m}}_{\mathrm{COND}}\, \mathrm{h}_{\mathrm{lv}}^{'} = \mathrm{k_l}\, \mathrm{A_s} \left(\frac{\mathrm{T_{sat}} - \mathrm{T_s}}{\mathrm{H(t)}}\right)$$

Equation 61

Where the height of the liquid from the cold plate is given by Equation 62.

$$\mathrm{H(t)} = \delta_{\mathrm{i}} + \delta(\mathrm{t})$$

Equation 62

$$\dot{\mathrm{m}}_{\mathrm{COND}} = \rho_{\mathrm{l}} \mathrm{A_s} \left(\frac{\mathrm{dH}}{\mathrm{dt}}\right)$$

Equation 63

Equation 64 is obtained by substituting Equation 63 into Equation 61.

$$\rho_l \cancel{A_s} \left(\frac{dH}{dt}\right) h'_{fg} = k_l \cancel{A_s} \left(\frac{T_{sat} - T_s}{H(t)}\right)$$

Equation 64

Rearranging Equation 64 , Equation 65 is obtained.

$$H\,dH = \frac{k_l\,(T_{sat} - T_s)}{h'_{lv}\,\rho_l}\,dt$$

Equation 65

Integrate Equation 65 to obtain Equation 67.

$$\int_{\delta_i}^{\delta_i+\delta} H\,dH = \frac{k_l\,(T_{sat} - T_s)}{h'_{lv}\,\rho_l} \int_0^t dt$$

Equation 66

$$\left[\frac{1}{2}(\delta_i + \delta)^2 - \frac{1}{2}(\delta_i)^2\right] = \frac{k_l\,(T_{sat} - T_s)}{h'_{lv}\,\rho_l}\,(t - 0)$$

Equation 67

Rearrange Equation 67 to obtain Equation 73.

$$\frac{1}{2}\left[\left({\delta_i}^2 + 2\delta_i\delta + \delta^2\right) - (\delta_i)^2\right] = \frac{k_l\,(T_{sat} - T_s)}{h'_{lv}\,\rho_l}\,t \qquad (68)$$

Equation 68

$$\left(2\delta_i\delta + \delta^2\right) + \delta_i^2 = \frac{2\,k_l\,(T_{sat} - T_s)}{h'_{lv}\,\rho_l}\,t + \delta_i^2 \qquad (69)$$

Equation 69

$$(\delta_i + \delta)^2 = \frac{2\,k_l\,(T_{sat} - T_s)}{h'_{lv}\,\rho_l}\,t + \delta_i^2 \qquad (70)$$

Equation 70

$$\delta_i + \delta = \sqrt{\frac{2\,k_l\,(T_{sat} - T_s)\,t}{h'_{lv}\,\rho_l} + \delta_i^2} \qquad (71)$$

Equation 71

$$\delta = \sqrt{\frac{2\,k_l\,(T_{sat} - T_s)\,t}{h'_{lv}\,\rho_l} + \delta_i^2} - \delta_i \qquad (72)$$

Equation 72

$$\delta = \sqrt{\frac{2\,k_l\,(T_{sat} - T_s)\,t + \delta_i^2\,h_{lv}\,\rho_l}{h_{lv}\,\rho_l}} - \delta_i \tag{73}$$

Equation 73

The general definition of the heat transfer coefficient is given by Equation 74.

$$h = \frac{k_l}{H(t)} = \frac{k_l}{\delta(t) + \delta_i} \tag{74}$$

Equation 74

Substitute Equation 73 into Equation 74 to obtain Equation 75, the derived heat transfer coefficient for condensation on flat, horizontal cold plate.

$$h = \frac{k_l}{\left[\sqrt{\frac{2\,k_l\,(T_{sat} - T_s)\,t + \delta_i^2\,h_{lv}\,\rho_l}{h_{lv}\,\rho_l}} - \delta_i\right] + \delta_i} \tag{75}$$

Equation 75

$$\boxed{h = k_l \sqrt{\frac{h_{lv}\,\rho_l}{2\,k_l\,(T_{sat} - T_s)\,t + \delta_i^2\,h_{lv}\,\rho_l}}} \tag{76}$$

Equation 76

The condensation mass flux is found by rearranging Equation 61.

$$G_{COND} = \frac{\dot{m}_{COND}}{A_s} = \frac{k_l}{h_{lv}}\left(\frac{T_{sat} - T_s}{H(t)}\right)$$

Equation 77

Substituting Equation 73 into Equation 77, gives the condensation mass flux, Equation 78.

$$G_{COND} = \frac{k_l}{h_{lv}^{'}} \frac{(T_{sat} - T_s)}{\left[\sqrt{\frac{2\,k_l\,(T_{sat} - T_s)\,t + \delta_i^2\,h_{lv}\,\rho_l}{h_{lv}\,\rho_l}} - \delta_i\right] + \delta_i}$$

Equation 78

$$G_{COND} = \frac{k_l}{h_{lv}^{'}} (T_{sat} - T_s) \sqrt{\frac{h_{lv}\,\rho_l}{2\,k_l\,(T_{sat} - T_s)\,t + \delta_i^2\,h_{lv}\,\rho_l}}$$

Equation 79

$$\boxed{G_{COND} = k_l (T_{sat} - T_s) \sqrt{\frac{\rho_l}{h_{lv}\left[2\ k_l\ (T_{sat} - T_s)\ t + \delta_i^2\ h_{lv}\ \rho_l\right]}}}$$

Equation 80

Direct Contact Condensation by Bubble Collapse

Bubble Departure Frequency Derivation

$$f_{b,d} = \frac{\dot{m}_{GO_2}}{m_{b,d}}$$

Equation 81

$$f_{b,d} = \frac{\dot{m}_{GO_2}}{\rho_v V_{b,d}}$$

Equation 82

$$f_{b,d} = \frac{\dot{m}_{GO_2}}{\rho_v \left[\frac{4}{3}\pi \left(\frac{D_{b,d}}{2}\right)^3\right]}$$

Equation 83

$$\boxed{f_{b,d} = \frac{6\ \dot{m}_{GO_2}}{\pi\ \rho_v\ D_{b,d}^3}}$$

Equation 84

Mass Condensation Rate of Bubble

$$\dot{m}_{b,cond} = \left[m_{b,cond}\right]\left[f_{b,d}\right]$$

Equation 85

$$\dot{m}_{b,cond} = \left[\frac{6\ \dot{m}_{GO_2}}{\pi\ \rho_v\ D_{b,d}^3}\right]\left[\rho_v \frac{4\pi}{3}\left(\frac{D_{b,d}}{2}\right)^3 - \rho_v \frac{4\pi}{3}\left(\frac{D_{t_r}}{2}\right)^3\right]$$

Equation 86

$$\dot{m}_{b,cond} = \left[\frac{\cancel{6}\ \dot{m}_{GO_2}}{\cancel{\pi\ \rho_v}\ D_{b,d}^3}\right]\left[\cancel{\rho_v} \frac{\cancel{\pi}}{\cancel{6}}\left({D_{b,d}}^3 - {D_{t_r}}^3\right)\right]$$

Equation 87

$$\dot{m}_{b,cond} = \dot{m}_{GO_2}\left(\frac{D_{b,d}{}^3 - D_{t_r}{}^3}{D_{b,d}{}^3}\right)$$

Equation 88

$$\dot{m}_{b,cond} = \dot{m}_{GO_2}\left[\left(\frac{D_{b,d}}{D_{b,d}}\right)^3 - \left(\frac{D_{t_r}}{D_{b,d}}\right)^3\right]$$

Equation 89

$$\boxed{\dot{m}_{b,cond} = \dot{m}_{GO_2}\left(1 - \beta_{t_r}{}^3\right)} \quad \text{where } \frac{D_{b,t_r}}{D_{b,d}} = \beta_{t_r}$$

Equation 90

$$\dot{m}_{COND} = \dot{m}_{b,COND} + \dot{m}_{ULL,COND}$$

$$\dot{m}_{COND} = \dot{m}_{COND}\left(1 - \beta_{t_r}{}^3\right) + G_{COND}A_{CS-IRAS}$$

$$\dot{m}_{COND} - \dot{m}_{COND}\left(1 - \beta_{t_r}{}^3\right) = \dot{m}_{COND}\left[1 - \left(1 - \beta_{t_r}{}^3\right)\right] = G_{COND}A_{CS-IRAS}$$

$$\dot{m}_{COND}\left(\beta_{t_r}\right) = G_{COND}A_{CS-IRAS}$$

$$\dot{m}_{COND} = \frac{G_{COND}A_{CS-IRAS}}{\beta_{t_r}}$$

Average Heat Transfer Coefficient

$$Nu_{b,d} = \frac{h\ D_{b,d}}{k_l} = \frac{1}{\sqrt{\pi}}\sqrt{\frac{\rho_l u_b D_{b,d}}{\mu_l}}\ Pr^{\frac{1}{3}}$$

Equation 91

$$Nu_{b,t_r} = \frac{h\ D_{b,t_r}}{k_l} = \frac{1}{\sqrt{\pi}}\sqrt{\frac{\rho_l u_b D_{b,t_r}}{\mu_l}}\ Pr^{\frac{1}{3}}$$

Equation 92

$$h_{avg} = \frac{k_L}{2\sqrt{\pi}}\sqrt{\frac{\rho_L u_b}{\mu_L}} Pr^{\frac{1}{3}}\left(\frac{1}{\sqrt{D_{b,d}}} + \frac{1}{\sqrt{D_{b,t_r}}}\right)$$

Equation 93

$$h_{avg} = \frac{k_l}{2\sqrt{\pi}}\sqrt{\frac{\rho_l u_b}{\mu_l}} Pr^{\frac{1}{3}}\left(\frac{1}{\sqrt{D_{b,d}}} + \frac{1}{\sqrt{D_{b,t_r}}}\right)\frac{\sqrt{D_{b,d}}}{\sqrt{D_{b,d}}}$$

Equation 94

$$h_{avg} = \frac{k_l}{2\sqrt{\pi}}\sqrt{\frac{\rho_l u_b D_{b,d}}{\mu_l}}\Pr^{\frac{1}{3}}\left(1+\frac{\sqrt{D_{b,d}}}{\sqrt{\overline{D_{b,t_r}}}}\right)$$

Equation 95

$$h_{avg} = \frac{k_l}{2\sqrt{\pi}}\sqrt{Re_{b,d}}\Pr^{\frac{1}{3}}\left(1+\frac{1}{\beta_{t_r}}\right)$$

Equation 96

$$\boxed{h_{avg} = \frac{k_l}{2\sqrt{\pi}}\sqrt{Re_{b,d}}\Pr^{\frac{1}{3}}\left(\frac{\beta_{t_r}+1}{\beta_{t_r}}\right)}$$

Equation 97

APPENDIX E: OXYGEN AND NITROGEN PROPERTY CORRELATIONS

Oxygen Vapor Pressure

Equation 98 and Equation 99 calculate the vapor pressure of oxygen at a given temperature [31].

$$\ln\left(\frac{P}{P_t}\right) = A\chi + B\chi^2 + C\chi^3 + D\chi(1-\chi)^{\varepsilon}$$

Equation 98

$$\chi = \frac{\left(1 - \frac{T_t}{T}\right)}{\left(1 - \frac{T_t}{T_c}\right)}$$

Equation 99

Where,

$A =$ 7.7977723

$B =$ 4.5773000

$C =$ -1.9281264

$D =$ 3.2931232

$\varepsilon =$ 1.5

$P_t =$ 0.001464 bar

$T_t =$ 54.359 K

$T_c =$ 154.581 K

Oxygen Vapor Heat Capacity

Equation 100 calculates the heat capacity of oxygen vapor [31].

$$\frac{c_{P,O_2}}{R} = \frac{A_1}{T^3} + \frac{A_2}{T^2} + \frac{A_3}{T} + A_4 + A_5 T + A_6 T^2 + A_7 T^3 + \frac{A_8 \left(\frac{A_9}{T}\right)^2 e^{\frac{A_9}{T}}}{\left(e^{\frac{A_9}{T}} - 1\right)^2}$$

Equation 100

Where,

$A_1 =$ $-1.86442361 \times 10^{2}$

$A_2 =$ 2.07840241×10^{1}

$A_3 =$ $-3.42642911 \times 10^{-1}$

$A_4 =$ 3.50297163×10^{0}

$A_5 =$ $2.05866482 \times 10^{-7}$

$A_6 =$ $-1.11035799 \times 10^{-8}$

$A_7 =$ $2.08612876 \times 10^{-11}$

$A_8 =$ 1.01894691×10^{0}

$A_9 =$ 2.23918105×10^{3}

Oxygen Vapor Density

Equation 101, Equation 102, and Equation 103 calculate the vapor density of oxygen at a given temperature and pressure [31].

$$P = T\,R\,\rho_{GO_2}\left(1 + B\,\rho_{GO_2} + C\,\rho_{GO_2}{}^{2}\right)$$

Equation 101

$$B = \sum_{j}^{5} B_j\,T^{\frac{1-j}{4}}$$

Equation 102

Where,

B_1 = -8.638001288 x 10^2
B_2 = 1.733064315 x 10^4
B_3 = -1.241961054 x 10^5
B_4 = 3.956609285 x 10^5
B_5 = -4.904475356 x 10^5

$$C = \sum_{j}^{6} C_j\,T^{\frac{1-j}{2}}$$

Equation 103

Where,

C_1 = 3.569552013 x 10^5
C_2 = -2.696578423 x 10^7
C_3 = 8.152809009 x 10^8
C_4 = -1.229796911 x 10^{10}
C_5 = 9.252345993 x 10^{10}
C_6 = -2.771904509 x 10^{11}

Oxygen Latent Heat

A third order polynomial curve was applied to data for oxygen latent heat obtained from Weber[31]. Equation 104 shows the third order polynomial curve from Excel. Figure 22 shows the thermal conductivity data with the plot of Equation 104.

$$h_{lv} = A + BT + CT^2 + DT^3$$

Equation 104

Where,

A = -0.000081397422873
B = 0.014733449692986
C = -1.651586006233110
D =301.861319160972000

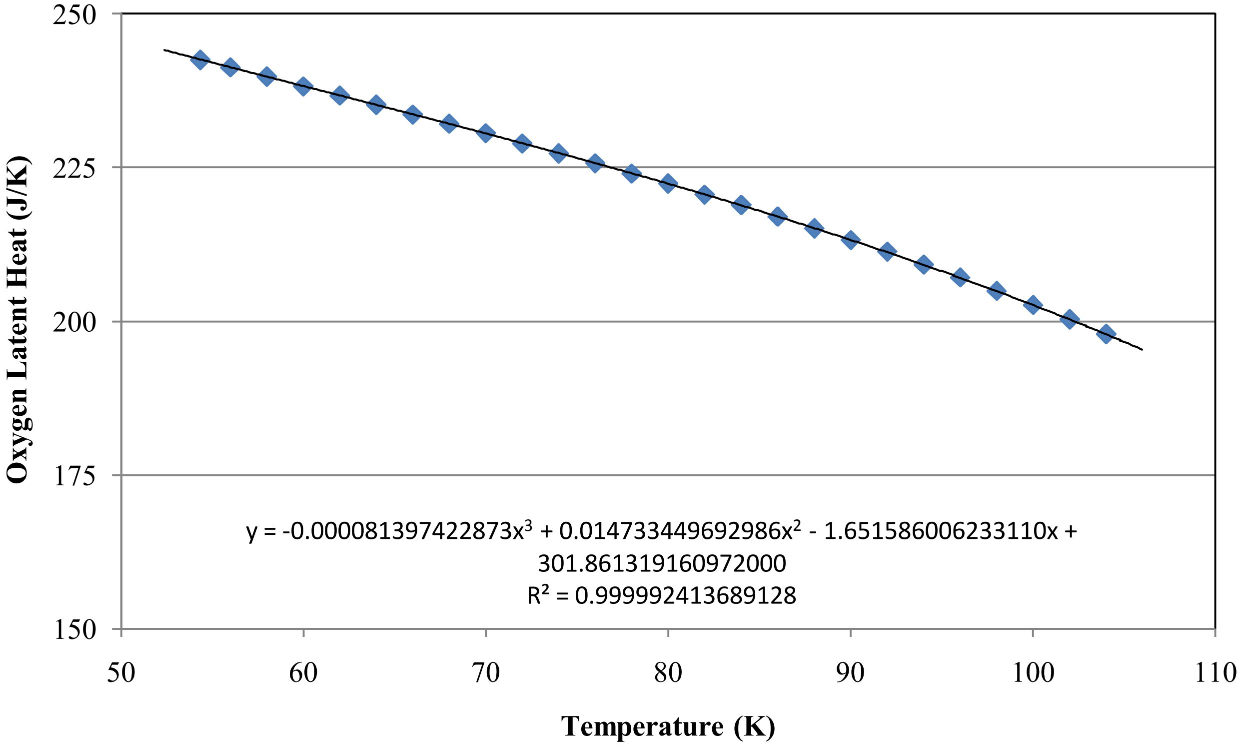

Figure 22: Oxygen Latent Heat

Liquid Oxygen Heat Capacity

A fifth order curve was applied to data for liquid oxygen density obtained from Barron [33]. Equation 105 shows the sixth order curve from Excel. Figure 23 shows the liquid oxygen density data with the plot of Equation 105.

$$c_{P,LO_2} = A + BT + CT^2 + DT^3 + ET^4 + FT^5$$

Equation 105

Where,

A = -804.941841795574000
B = 157.662398397089000
C = -3.989099267857940
D = 0.049706461920543
E = -0.000304345673485
F = 0.000000737635884

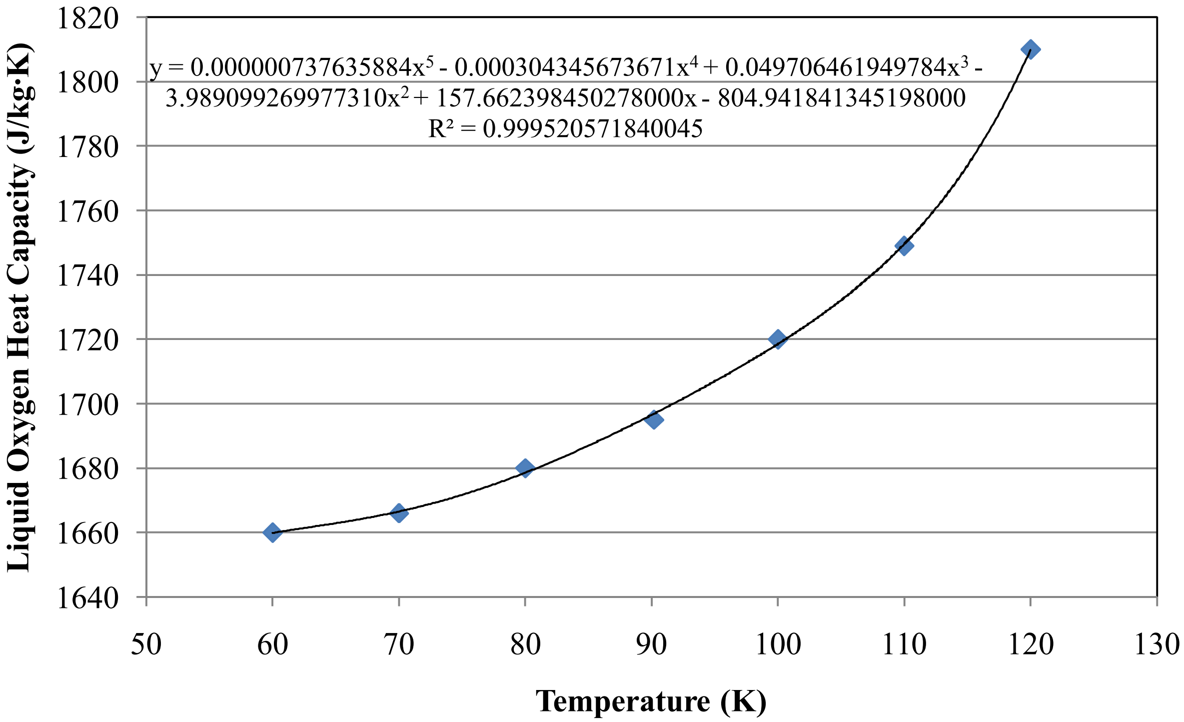

Figure 23: Liquid Oxygen Heat Capacity

Liquid Oxygen Density

A sixth order curve was applied to data for liquid oxygen density obtained from Weber [31]. Equation 106 shows the sixth order curve from Excel. Figure 24 shows the liquid oxygen density data with the plot of Equation 106.

$$\rho_{LO_2} = A + BT + CT^2 + DT^3 + ET^4 + FT^5 + GT^6$$

Equation 106

Where,

A = 1,828.148354159390000
B = -24.432705431840600
C = 0.601754991149983
D = -0.009840755672421
E = 0.000092502281069
F = -0.000000472160225
G = 0.000000001000684

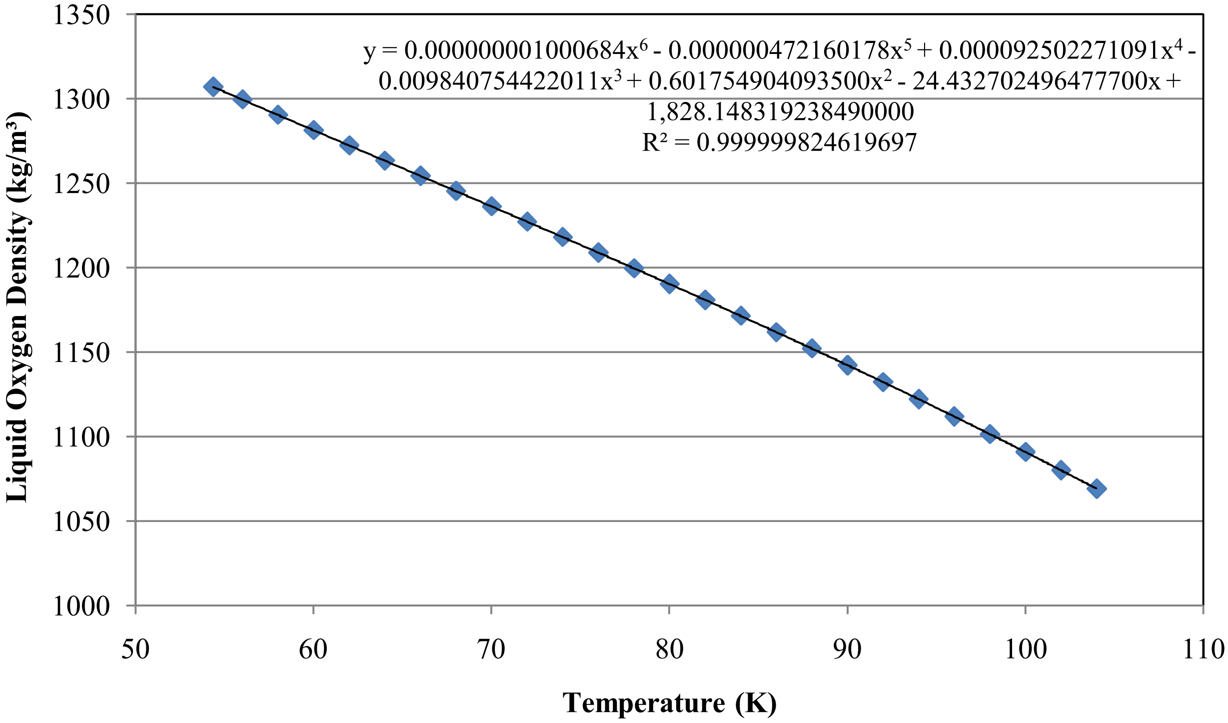

Figure 24: Liquid Oxygen Density

Liquid Oxygen Thermal Conductivity

A third order polynomial curve was applied to data for liquid oxygen thermal conductivity obtained from Barron [32]. Equation 107 shows the third order polynomial curve from Excel. Figure 25 shows the thermal conductivity data with the plot of Equation 107.

$$k_L = A + BT + CT^2 + DT^3$$

Equation 107

Where,

A = 0.213338803988351
B = 0.000289487448988
C = - 0.000014585678268
D = 0.000000041651737

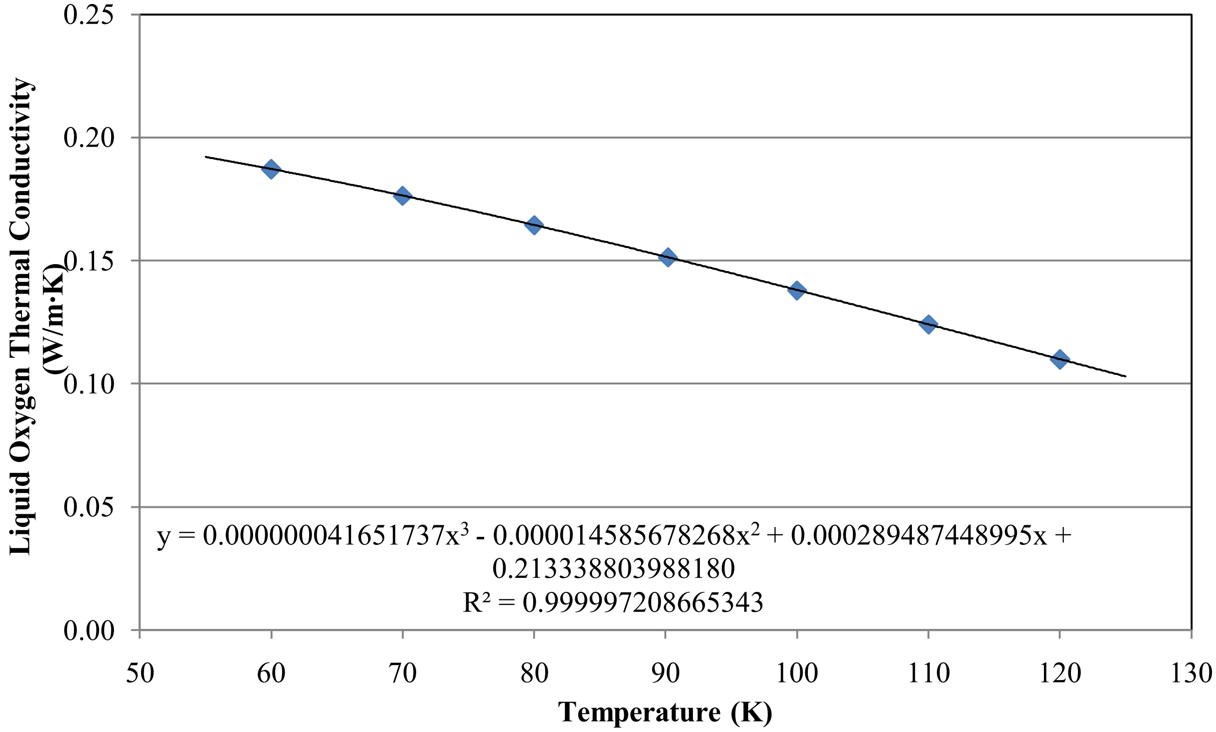

Figure 25: Liquid Oxygen Thermal Conductivity

Liquid Oxygen Viscosity

A fifth order polynomial curve was applied to data for liquid oxygen viscosity obtained from Barron [32]. Equation 108 shows the third order polynomial curve from Excel. Figure 26 shows the thermal conductivity data with the plot of Equation 108.

$$\mu_{LO_2} = A + BT + CT^2 + DT^3 + ET^4 + FT^5$$

Equation 108

Where,

A = 0.01471506017385700000000000
B = - 0.00065484899149639500000000
C = 0.00001201046285763370000000
D = - 0.00000011122794352825600000
E = 0.00000000051581996648269300
F = -0.00000000000095362943927490

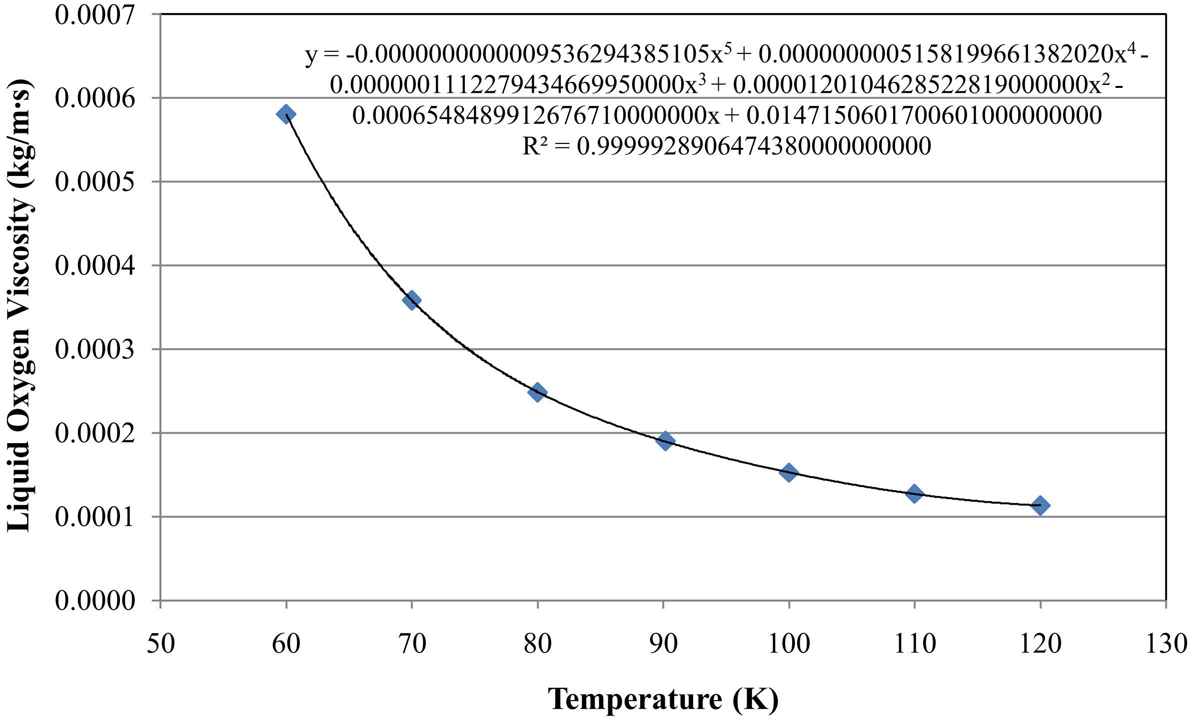

Figure 26: Liquid Oxygen Viscosity

Liquid Oxygen Surface Tension

A third order polynomial curve was applied to data for liquid oxygen surface tension obtained from Barron [32]. Equation 109 shows the third order polynomial curve from Excel. Figure 27 shows the surface tension data with Equation 109.

$$\sigma_L = A + BT + CT^2 + DT^3$$

Equation 109

Where,

A = 0.03784273362256790000
B = - 0.00028019982284562800
C = - 0.00000009855225489719
D = 0.00000000194328853049

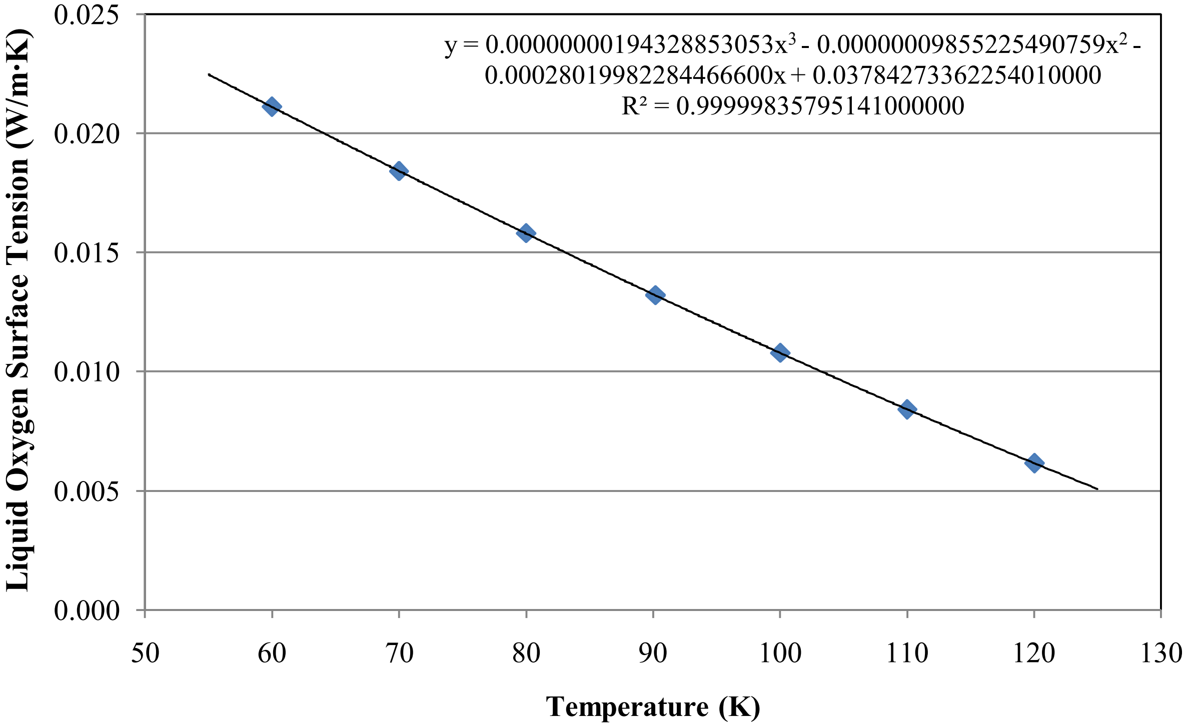

Figure 27: Liquid Oxygen Surface Tension

Nitrogen Vapor Pressure

Equation 110 calculates the vapor pressure of nitrogen at a given temperature [33].

$$\ln(\mathrm{P}) = \frac{\mathrm{N_1}}{\mathrm{T}} + \mathrm{N_2} + \mathrm{N_3T} + \mathrm{N_4}(\mathrm{T_c} - \mathrm{T})^{1.95} + \mathrm{N_5T^3} + \mathrm{N_6T^4} + \mathrm{N_7T^5} + \mathrm{N_8T^6} + \mathrm{N_9}\ln(\mathrm{T})$$

Equation 110

Where,

$N_1 = 0.8394409444 \times 10^{4}$
$N_2 = -0.1890045259 \times 10^{4}$
$N_3 = -0.7282229165 \times 10^{1}$
$N_4 = 0.1022850966 \times 10^{-1}$
$N_5 = 0.5556063825 \times 10^{-3}$
$N_6 = -0.5944544662 \times 10^{-5}$
$N_7 = 0.2715433932 \times 10^{-7}$
$N_8 = -0.4879535901 \times 10^{-10}$
$N_9 = 0.5095360824 \times 10^{3}$

Nitrogen Vapor Heat Capacity

Equation 111 calculates the heat capacity of nitrogen vapor [33].

$$\frac{c_{P,N_2}}{R} = \frac{N_1}{T^3} + \frac{N_2}{T^2} + \frac{N_3}{T} + N_4 + N_5T + N_6T^2 + N_7T^3 + \frac{N_8\left(\frac{N_9}{T}\right)^2 e^{\frac{N_9}{T}}}{\left(e^{\frac{N_9}{T}} - 1\right)^2}$$

Equation 111

Where,

$N_1 = -0.7352104012 \times 10^{3}$
$N_2 = 0.3422399804 \times 10^{2}$
$N_3 = -0.5576482846 \times 10^{0}$
$N_4 = 0.3504042283 \times 10^{1}$
$N_5 = -0.1733901851 \times 10^{-4}$
$N_6 = 0.1746508498 \times 10^{-7}$
$N_7 = -0.3568920335 \times 10^{-11}$
$N_8 = 0.1005387228 \times 10^{1}$
$N_9 = 3353.4061$

Nitrogen Latent Heat

A sixth order polynomial curve was applied to data for nitrogen latent heat obtained from Jacobsen and Stewart [33]. Equation 112 shows the sixth order polynomial curve from Excel. Figure 28 shows the thermal conductivity data with the plot of Equation 112.

$$h_{lv} = A + BT + CT^2 + DT^3 + ET^4 + FT^5 + GT^6$$

Equation 112

Where,

A = -2948.433966063970000
B = 227.928493462180000
C = -6.728937040380770
D = 0.104914396711496
E = -0.000915160992150
F = 0.000004235559605
G = -0.000000008148664

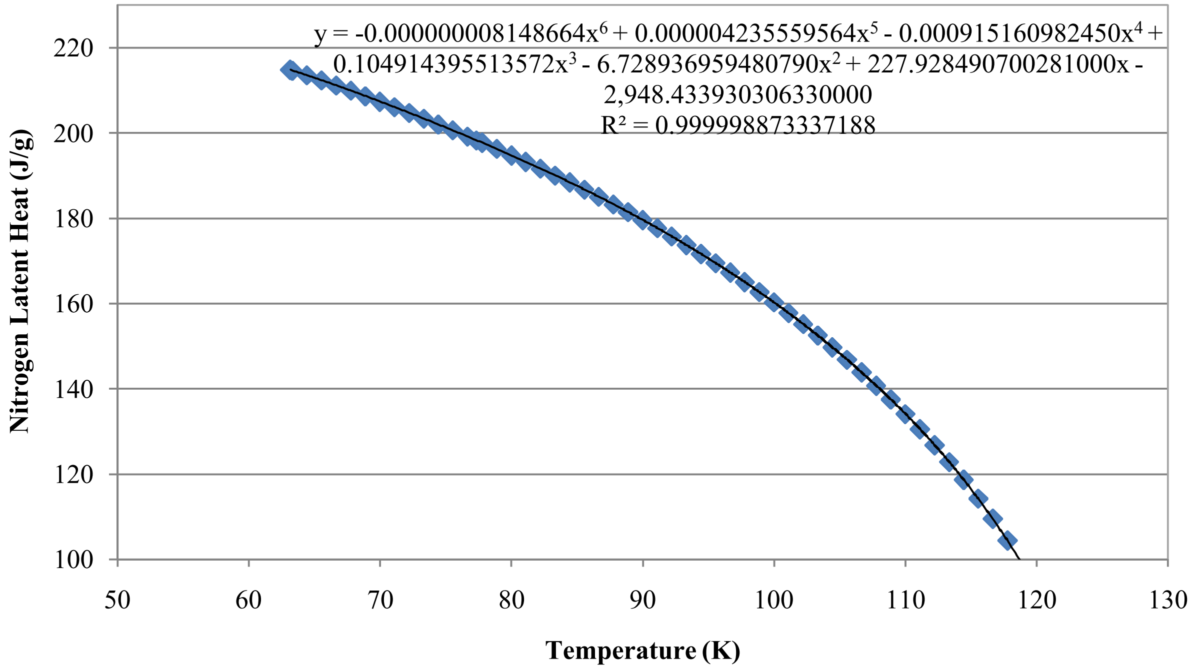

Figure 28: Nitrogen Latent Heat

Liquid Nitrogen Density

A sixth order polynomial curve was applied to data for liquid nitrogen density obtained from Jacobsen and Stewart [33]. Equation 113 shows the sixth order polynomial curve from Excel. Figure 29 shows the thermal conductivity data with the plot of Equation 113.

$$\rho_{LN_2} = A + BT + CT^2 + DT^3 + ET^4 + FT^5 + GT^6$$

Equation 113

Where,

A = -5,400.668730378720000
B = 454.403865170203000
C = - 13.412411829511900
D = 0.208986234251856
E = - 0.001826834840131
F = 0.000008485691357
G = -0.000000016386729

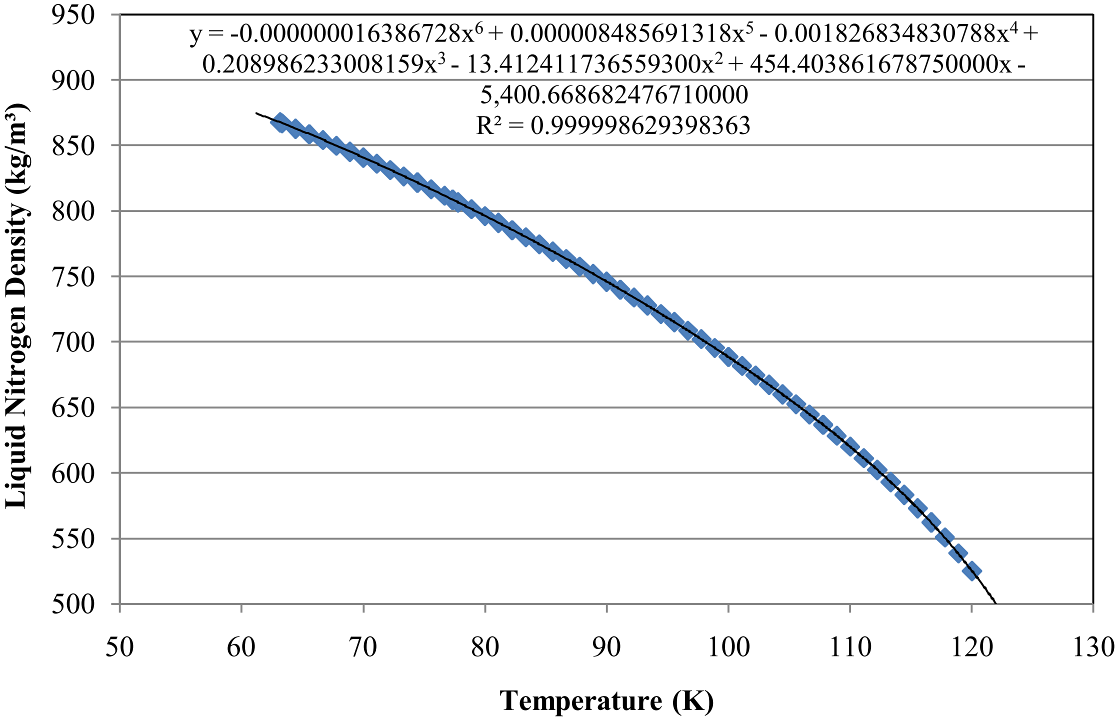

Figure 29: Liquid Nitrogen Density

Helium Solubility in Liquid Oxygen

Normally, the ullage gas is composed of the same component as the liquid in cryogenic systems. When the ullage gas is replaced with a non-condensable, a portion of the non-condensable gas is absorbed into the liquid. The non-condensable gas, helium, is used in the IRAS densification runs. The amount of non-condensable gas that is absorbed in the liquid is a function of the relative volatility and the system pressure. The relative volatility is the volatility of the non-condensable gas compared to the volatility of the liquid. Equation 114 through Equation 117 provide the correlation of helium solubility in liquid oxygen as a function of temperature and pressure.

$$x = P^{*}\exp(a(T) + b(T)P^{*})$$

Equation 114

$$a(T) = a_0 + a_1T + a_2T^2$$

Equation 115

$$b(T) = b_0 + b_1T + b_2T^2$$

Equation 116

$$P^{*} = \left(\frac{P - P_V}{P_{ref}}\right)$$

Equation 117

Where

$a_0 = -13.82$

$a_1 = 0.0934/K$

$a_2 = -0.00021/K^2$

$b_0 = 0$

$b_1 = 0/K$

$b_2 = 0/K^2$

APPENDIX F: SAMPLE CALCULATIONS

Equation 1

$$G_{COND} = \left(\frac{M}{2\pi R_u T}\right)^{\frac{1}{2}} \left[P_g - P_{sat}\right]$$

The molecular weight of oxygen is 0.032 kg/mol. The universal gas constant is 8.314 J/mol·K. The sample calculation for Equation 1 uses a liquid temperature of 94K at a IRAS system pressure of 7 psig. Equation 98 estimates the saturated pressure at a temperature of 94K.

$$G_{COND} = \left(\frac{0.032\frac{kg}{mol}}{2\pi\left(8.314\frac{J}{mol \cdot K}\right)94K}\right)^{\frac{1}{2}} [149{,}588Pa - 148{,}353Pa]$$

$$\boxed{G_{COND} = 3.153\frac{kg}{s \cdot m^2}}$$

Equation 2

$$h = \left(\frac{M}{2\pi R_u T}\right)^{\frac{1}{2}} \frac{h_{lv}^2}{T\, v_{lv}}$$

The components inside the parenthesis have been addressed in the Equation 1 sample calculation. Equation 104 estimates the latent heat at a temperature of 94K, while the difference between the reciprocals of Equation 101 and Equation 106 provides the specific volume change from vapor to liquid.

$$h = \left(\frac{0.032\frac{kg}{mol}}{2\pi\left(8.314\frac{J}{mol \cdot K}\right)94K}\right)^{\frac{1}{2}} \frac{\left[209{,}190\frac{J}{kg}\right]^2}{(94K)\left[\frac{1}{4.127\frac{kg}{m^3}} - \frac{1}{1122.252\frac{kg}{m^3}}\right]}$$

$$\boxed{h = 5{,}097\frac{kW}{m^2 \cdot K}}$$

Equation 3

$$G_{COND} = \left(\frac{M}{2\pi R_u T}\right)^{\frac{1}{2}} \left[\Gamma(a)\sigma_c P_v - \sigma_e P_g\right]$$

The components inside the parenthesis and the two pressures were determined in the two above sample calculations. The condensation coefficient, σ_c, and evaporation coefficient, σ_e, are set equal to 1. The function, $\Gamma(a)$, is determined by Equation 4 and Equation 5 by iterative calculation with Equation 3 using Microsoft Excel. For this sample calculation, assume G_{COND} equals 0.24 kg/m²·s.

Equation 5

$$a = \frac{G_{COND}}{P_g}\sqrt{\frac{R\,T}{2\,M}} = \frac{0.24\frac{kg}{m^2\cdot s}}{149{,}588Pa}\sqrt{\frac{\left(8.314\frac{J}{mol\cdot K}\right)(94K)}{2\left(0.032\frac{kg}{mol}\right)}} = 0.005$$

Equation 4

$$\Gamma(a) = \exp(-a^2) + a\sqrt{\pi}[1 + erf(a)] = \exp(-(0.005)^2)(0.005)\sqrt{\pi}[1 + erf(0.005)]$$

$$\Gamma(a) = 1.0089$$

$$G_{COND} = \left(\frac{0.032\frac{kg}{mol}}{2\pi\left(8.314\frac{J}{mol\cdot K}\right)94K}\right)^{\frac{1}{2}}[(1.0089)(1)149{,}588Pa - (1)148{,}353Pa]$$

$$\boxed{G_{COND} = 0.24\frac{kg}{m^2\cdot s}}$$

No need to continue with iterations, since condensation mass flux agrees with assumption.

Equation 6

$$G_{COND} = k_l(T_{sat} - T_s)\sqrt{\frac{\rho_l}{h_{lv}[2\,k_l\,(T_{sat} - T_s)\,t + \delta_i^2\,h_{lv}\,\rho_l]}}$$

The latent heat (h_{lv}), liquid oxygen density (ρ_l), and thermal conductivity (k_l) are determined by Equation 104, Equation 106, and Equation 107. For the purposes of this sample calculation, the saturated temperature is 94K, with an IRAS heat exchanger surface of temperature of 85K, a liquid height of 12 inches above the heat exchanger, and an elapsed time of 10 seconds.

$$G_{COND} = k_l(T_{sat} - T_s)\sqrt{\frac{\rho_l}{h_{lv}\left[2\,k_l\,(T_{sat} - T_s)\,t + \delta_i^2\,h_{lv}\,\rho_l\right]}}$$

$$G_{COND} = \left(0.1463\frac{W}{m \cdot K}\right)(94K - 85K) \cdot \sqrt{\frac{1122\frac{kg}{m^3}}{\left(209{,}190\frac{J}{kg}\right)\left[2\left(0.1463\frac{W}{m \cdot K}\right)(94K - 85K)(10s) + (0.305m)^2\left(209{,}190\frac{J}{kg}\right)\left(1122\frac{kg}{m^3}\right)\right]}}$$

$$\boxed{G_{COND} = 3.215x10^{-5}\,\frac{kg}{m^2 \cdot s}}$$

Equation 7

$$h = k_l\sqrt{\frac{h_{lv}\,\rho_l}{2\,k_l\,(T_{sat} - T_s)\,t + \delta_i^2\,h_{lv}\,\rho_l}}$$

The sample calculation for Equation 6 provides the values for each of the components in Equation 7.

$$h = \left(0.1463\frac{W}{m \cdot K}\right) \cdot \sqrt{\frac{\left(209{,}190\frac{J}{kg}\right)\left(1122\frac{kg}{m^3}\right)}{\left[2\left(0.1463\frac{W}{m \cdot K}\right)(94K - 85K)(10s) + (0.305m)^2\left(209{,}190\frac{J}{kg}\right)\left(1122\frac{kg}{m^3}\right)\right]}}$$

$$\boxed{h = 5.75\,\frac{W}{m^2 \cdot s}}$$

Equation 8

$$D_d = \sqrt[3]{\frac{6\,\sigma\,D_n}{\rho_{lv}\,g}}$$

The sample calculation below uses Equation 109 to estimate the liquid oxygen surface tension. The nozzle diameter is the inner diameter of the liquid oxygen fill tube, which is a 0.500” x 0.049” and downstream of HV-1. The difference between the liquid density and vapor density is obtained from Equation 106 and Equation 101, respectively, at a liquid oxygen temperature of 94K.

$$D_d = \sqrt[3]{\frac{6\left[0.01225\frac{N}{m}\right]\left[0.010211m\right]}{\left[1122.2\frac{kg}{m^3} - 4.273\frac{kg}{m^3}\right]\left[9.81\frac{m}{s^2}\right]}}$$

$$\boxed{D_d = 0.00409m}$$

Equation 9

$$\beta = \left(1 - \frac{3}{\sqrt{\pi}}\,Ja\,\sqrt{Re_{bo}}\,Pr^{\frac{1}{3}}\,Fo_o\right)^{\frac{2}{3}} = \left(1 - \frac{3}{\sqrt{\pi}}\,\frac{\rho_f c_p (T_{sat} - T_f)}{\rho_g h_{fg}}\,\sqrt{\frac{\rho_l u_b D_d}{\mu_l}}\,Pr^{\frac{1}{3}}\,\frac{\alpha\,t_r}{D_d^2}\right)^{\frac{2}{3}}$$

The sample calculation below uses Equation 106, Equation 105, Equation 98, Equation 101, Equation 104, and Equation 108 to estimate the liquid density, liquid specific heat capacity, saturation temperature, vapor density, latent heat, liquid viscosity, respectively, evaluated at a temperature of 94K and a pressure of 7 psig. The bubble velocity, u_b, and departure diameter, D_d, are determined by the sample calculations for Equation 8 and Equation 10.

$$Ja = \frac{\rho_f c_p (T_{sat} - T_f)}{\rho_g h_{fg}} = \frac{\left(1122.2\frac{kg}{m^3}\right)\left(1.705\frac{kJ}{kg \cdot K}\right)(94.09K - 94K)}{\left(4.273\frac{kg}{m^3}\right)\left(209.2\frac{kJ}{kg}\right)} = 0.1291$$

$$Re_{bo} = \frac{\rho_l u_b D_d}{\mu_l} = \frac{\left(1122.2\frac{kg}{m^3}\right)\left(0.1554\frac{m}{s}\right)(0.003615m)}{\left(0.000173\frac{kg}{m \cdot s}\right)} = 4115.8$$

$$\mathrm{Pr} = \frac{c_{p,l}\mu_l}{k_l} = \frac{\left(1704.8\,\frac{J}{kg\cdot K}\right)\left(0.000173\,\frac{kg}{m\cdot s}\right)}{\left(0.1463\,\frac{W}{m\cdot K}\right)} = 2.012$$

$$\beta = \left(1 - \frac{3}{\sqrt{\pi}}\,(0.1291)\,\sqrt{(4115.8)}\,(2.012)^{\frac{1}{3}}\,\frac{\left(7.645\mathrm{x}10^{-8}\,\frac{m^2}{s}\right)(5.88s)}{(0.003615m)^2}\right)^{\frac{2}{3}}$$

$$\boxed{\beta = 0.65}$$

Equation 10

$$U_b = \frac{C_z}{1-\alpha}\left(\frac{g\,\sigma\,\rho_{fg}}{\rho_f^2}\right)^{\frac{1}{4}} = \frac{1.53}{1-0}\left(\frac{\left[9.81\,\frac{m}{s^2}\right]\left[0.01225\,\frac{N}{m}\right]\left[1122.2\,\frac{kg}{m^3} - 4.273\,\frac{kg}{m^3}\right]}{\left[1122.2\,\frac{kg}{m^3}\right]^2}\right)^{\frac{1}{4}} =$$

$$\boxed{U_b = 0.1554\,\frac{m}{s}}$$

Equation 12

$$t_r = \frac{H}{u_b} = \frac{0.9144m}{0.1554\,\frac{m}{s}}$$

Assume H = 36 inches or 0.9144 m and the upward velocity, u_b, is provided by the result of Equation 10 sample calculation.

$$\boxed{t_r = 5.88s}$$

Equation 14

$$f_{b,d} = \frac{6\,\dot{m}_{GO_2}}{\pi\,\rho_v\,D_{b,d}^3}$$

Assume the gaseous oxygen mass flow rate is 2 sLm. The oxygen vapor density is estimated by Equation 101, assuming a vapor temperature of 200 K. Although the oxygen vapor originates in k-bottle at ambient temperature, the oxygen vapor flows through ½” stainless steel tubing through the IRAS dewar to the bottom of the IRAS dewar. As the gaseous oxygen flows through the tubing, the oxygen cools. Sample calculations of Equation 8 gives the value for the bubble departure diameter, $D_{b,d}$.

$$f_{b,d} = \frac{6\ (2\ \mathrm{sLm})\left(\frac{0.001326\ \mathrm{kg}}{\mathrm{sL}}\right)\left(\frac{\mathrm{min}}{60\mathrm{s}}\right)}{\pi\left(1.955\frac{\mathrm{kg}}{\mathrm{m}^3}\right)(0.00409\mathrm{m})^3}$$

$$\boxed{f_{b,d} = \frac{631.24}{\mathrm{s}}}$$

Equation 28

$$\frac{P}{P_i} = \left[1 + \left(\frac{\gamma - 1}{2}\right)\left(\frac{2}{\gamma + 1}\right)^{\frac{(\gamma+1)}{2(\gamma-1)}}\sqrt{\frac{\gamma\, g_0 P_i}{\rho_i}}\ \frac{A\,t}{V}\right]^{\frac{-2\gamma}{(\gamma-1)}}$$

Rearrange to solve for the area (A).

$$A = \left(\frac{2}{\gamma - 1}\right)\left(\frac{\gamma + 1}{2}\right)^{\frac{(\gamma+1)}{2(\gamma-1)}}\sqrt{\frac{\rho_i}{\gamma\, g_0\, P_i}}\ \frac{V}{t}\left[\left(\frac{P}{P_i}\right)^{\frac{-(\gamma-1)}{2\gamma}} - 1\right]$$

For IRAS heat exchanger leak check, a gaseous helium at an initial pressure of 25.2378 psig (275,333 Pa) decayed to a final pressure of 24.7485 psig (271,959 Pa) in 1,110 seconds. The specific heat ratio of helium is 1.67 and the initial density of gaseous helium is 2.226 kg/m³. The gaseous helium occupies approximately 0.000445 m³ inside the IRAS heat exchanger.

$$A = \left(\frac{2}{1.67 - 1}\right)\left(\frac{1.67 + 1}{2}\right)^{\frac{(1.67+1)}{2(1.67-1)}}\sqrt{\frac{2.226\frac{\mathrm{kg}}{\mathrm{m}^3}}{1.67(275{,}333\mathrm{Pa})}}\ \frac{4.45\mathrm{x}10^{-4}\mathrm{m}^3}{1110\ \mathrm{s}}\left[\left(\frac{271{,}959\mathrm{Pa}}{275{,}333\mathrm{Pa}}\right)^{\frac{-(1.67-1)}{2(1.67)}} - 1\right]$$

$$\boxed{A = 5.43\mathrm{x}10^{-12}\mathrm{m}^2}$$

Equation 29

$$\frac{P}{P_i} = \exp\left[-\left(\frac{\gamma - 1}{2}\right)\left(\frac{2}{\gamma + 1}\right)^{\frac{(\gamma+1)}{2(\gamma-1)}} \sqrt{\frac{\gamma\, g_0 P_i}{\rho_i}}\ \frac{A\,t}{V}\right]$$

Rearrange to solve for area (A).

$$A = -\left(\frac{2}{\gamma - 1}\right)\left(\frac{\gamma + 1}{2}\right)^{\frac{(\gamma+1)}{2(\gamma-1)}} \sqrt{\frac{\rho_i}{\gamma\, g_0\, P_i}}\ \frac{V}{t}\ \ln\left(\frac{P}{P_i}\right)$$

$$A = -\left(\frac{2}{1.67 - 1}\right)\left(\frac{1.67 + 1}{2}\right)^{\frac{(1.67+1)}{2(1.67-1)}} \sqrt{\frac{2.226\,\frac{\text{kg}}{\text{m}^3}}{1.67(275{,}333\text{Pa})}}\ \frac{4.45\text{x}10^{-4}\text{m}^3}{1110\text{ s}}\ \ln\left[\frac{271{,}959\text{Pa}}{275{,}333\text{Pa}}\right]$$

$$\boxed{A = 2.70\text{x}10^{-11}\text{m}^2}$$

Equation 30

$$\dot{m} = C_D\, A \sqrt{2\, \Delta P\, \rho\, g_c}$$

The below sample calculation uses the Isentropic Blowdown area result from Equation 28, the liquid nitrogen mass flow rate through the leak. From orifice flow calculations, C_D ranges from a minimum of 0.54 to a maximum of unity [29], thus, the below sample calculation uses C_D equal to 1.00 to represent a maximum liquid nitrogen flowing through the leak in place of an uncertain C_D. The pressure difference (ΔP) is from the pressure of the liquid nitrogen flowing through the IRAS heat exchanger at 45 psig (411,588Paa) to the pressure within the IRAS dewar of 3 psig (122,588 Paa). The density of the liquid nitrogen is estimated from Equation 113 at a temperature of 80K.

$$\dot{m} = (1.00)\,(5.43\text{x}10^{-12}\text{m}^2) \sqrt{2\,(411{,}588\,\cancel{\text{Pa}} - 122{,}010\,\cancel{\text{Pa}})\left(796.23\frac{\text{kg}}{\text{m}^3}\right)\left(\frac{\frac{\cancel{\text{N}}}{\text{m}^2}}{\cancel{\text{Pa}}}\right)\left(\frac{\text{kg}\frac{\text{m}}{\text{s}^2}}{\cancel{\text{N}}}\right)}$$

$$\boxed{\dot{m} = 1.40\text{x}10^{-7}\,\frac{\text{kg}}{\text{s}} = 0.0072\text{sLm}}$$

Equation 31

$$Q_{EVAP} = \dot{m}\left[\int_{T_i}^{T_{BP}} c_{P,L}dT + h_{LV} + \int_{T_{BP}}^{T_f} c_{P,V}dT\right]$$

From Equation 112, $h_{LV}(T) = h_{LV}(77.3K) = 85.44\frac{J}{g}$

From Equation 111,

$$\int_{T_{BP}}^{T_f} c_{P,V}dT = \int_{77.3K}^{160K} R\left[\frac{N_1}{T^3} + \frac{N_2}{T^2} + \frac{N_3}{T} + N_4 + N_5T + N_6T^2 + N_7T^3 + \frac{N_8\left(\frac{N_9}{T}\right)^2 e^{\frac{N_9}{T}}}{\left(e^{\frac{N_9}{T}} - 1\right)^2}\right]dT$$

$$= R\left[-\frac{N_1}{4T^4} - \frac{N_2}{3T^3} + N_3\ln T + N_4T + \frac{N_5T^2}{2} + \frac{N_6T^3}{3} + \frac{N_7T^4}{4} + \frac{N_8N_9}{\left(e^{\frac{N_9}{T}} - 1\right)}\right]$$

$$= 85.79\frac{J}{g}$$

$$Q_{EVAP} = \dot{m}\left[\int_{T_i}^{T_{BP}} c_{P,L}dT + h_{LV} + \int_{T_{BP}}^{T_f} c_{P,V}dT\right] = \dot{m}\left[h_{LV} + \int_{T_{BP}}^{T_f} c_{P,V}dT\right]$$

$$= \dot{m}\left[h_{LV} + \int_{T_{BP}}^{T_f} c_{P,V}dT\right] = 5.3sLm\left(\frac{1.1614\,g}{sL}\right)\left(\frac{min}{60s}\right)\left[85.44\frac{J}{g} + 85.79\frac{J}{g}\right]$$

$$\boxed{Q_{EVAP} = 17.57W}$$

REFERENCES

[1] Thomas M. Flynn, Cryogenic Engineering, Marcel Dekker, New York, NY, 2005.

[2] Jerry Jon Sellers, Williams J. Astore, et al., Understanding Space, McGraw-Hill, Boston, MA, 2004.

[3] Pratt & Whitney Press Releases, Renowned Rocket Engine Celebrates 40 Years of Flight, Accessed: August 2, 2010, Published: November 24, 2003, http://www.pratt-whitney.com/vgn-ext-templating/v/index.jsp?vgnextoid=cabbe002c2f3c010VgnVCM1000000881000aRCRD&vgnextchannel=7dfc34890cb06110VgnVCM1000004601000aRCRD&vgnextfmt=default.

[4] Frank G. Kerry, Industrial Gas Handbook: Gas Separation and Purification, CRC Press, Boca Raton. FL, 2007.

[5] Conceptual Design of a Lunar Oxygen Pilot Plant, NASA Contract Number NA9-17878 EEI Report 88-182, NASA Johnson Space Center, Houston, TX, 1988.

[6] L.J. Hastings, D. W. Plachta, et al., An Overview of NASA Efforts on Zero Boiloff of Cryogenic Propellants, Cryogenics () (2002) 833-839.

[7] Charles Panzarella, David Plachta, et al., Pressure Control of Large Cryogenic Tanks in Microgravity, Cryogenics () (2004) 475-483.

[8] R. Hendricks, Paramagnetic Propellant Orientation, AIAA-91-2325, AIAA, Washington, D.C., 1991.

[9] Reduction of Liquid Hydrogen Boiloff Reliquefaction Cycle Analysis (MCR-76-229), Final Report, Martin Marietta, Denver, CO, 1976.

[10] Reduction of Liquid Hydrogen Boiloff: Optimal Reliquefaction System Design and Cost Study (MCR-77-136), Final Report, Martin Marietta, Denver, CO, 1978.

[11] J. R. Feller, Study of Large-Scale Zero Boil-Off Options for Launch Pad Storage of Cryogenic Propellants, Final Report, NASA-Ames Research Center, Moffet Field, CA, 2006.

[12] D.W. Plachta, R.J. Christie, et al., Passive ZBO Storage of Liquid Hydrogen and Liquid Oxygen Applied to Space Science Mission Concepts, Cryogenics () (2006) 89-97.

[13] NASA, The James Webb Space Telescope, , Accessed: June 7, 2010, Published: , , http://www.jwst.nasa.gov/observatory.html.

[14] R.G. Ross Jr., R. F. Boyle, An Overview of NASA Space Cryocooler Programs - 2006, International Cryocooler Conference, Annapolis, MD, 2006.

[15] Thomas M. Tomsik, Performance Tests of a Liquid Hydrogen Propellant Densification Ground Support System for the X33/RLV, AIAA () (1997) 2976-2992.

[16] T.I. Lak, M.E. Lozano, et al., Propellant Densification Without Use of Rotating Machinery, AIAA () (2002) 3599-3608.

[17] M. M. Fazah, STS Propellant Densification Feasibility Study Data Book, NASA Technical Memorandum 108467, NASA, Marshall Space Flight Center, AL, 1994.

[18] Frank P. Incropera, David P. Dewitt, Fundamentals of Heat and Mass Transfer, John Wiley & Sons, Hoboken, NJ, 2002.

[19] John G. Collier, Convective Boiling and Condensation, McGraw-Hill, Maidenhead, England, 1981.

[20] Y.M Chen, F. Mayinger, Measurement of Heat Transfer at the Phase Interface of Condensing Bubbles, International Journal of Multiphase Flow () (1992) 877-890.

[21] Jerrold Isenberg, David Moalem, et al., Direct Contact Heat Transfer with Change of Phase: Bubble Collapse with Translatory Motion in Single and Two Component Systems, International Journal of Heat Transfer () (1970) 997-1011.

[22] Y. Lerner, H. Kalman, et al., Condensation of an Accelerating-Decelerating Bubble: Experimental and Phenomenological Analysis, Journal of Heat Transfer () (1987) 509-517.

[23] O. Zeitoun, M. Shoukri, et al., Interfacial Heat Transfer Between Steam Bubbles and Subcooled Water in Vertical Upward Flow, Journal of Heat Transfer () (1995) 402-407.

[24] H. Kalman, Y.H. Mori, Experimental Analysis of a Single Vapor Bubble Condensing in Subcooled Liquid, Chemical Engineering Journal () (2002) 197-206.

[25] William U. Notardonato, Wesley L. Johnson, et al., Experimental Results of Integrated Refrigeration and Storage System Testing, in: Advances in Cryogenic Engineering, American Institute of Physics, Melville, NY, 2009, pp. 1369-1376.

[26] William U. Notardonato, Wesley L. Johnson, et al.,Integrated Refrigeration and Storage System - Heat Exchanger Characterization, Final Report, NASA, Kennedy Space Center, 2009.

[27] Matthew Nugent, Jared Sass, In-Situ Evaporator Propellant Conditioning - Test Report and Trade Study, ASRC Aerospace, Kennedy Space Center, 2009.

[28] Fredrick J. Moody, Introduction to Unsteady Thermofluid Mechanics, John Wiley & Sons, Inc., New York, 1990.

[29] Micheal R. Lindeburg, Mechanical Engineering Reference Manual, Ninth Edition, Professional Publications, Inc., Belmont, CA, 1995, pp. 3-22 - 3-23.

[30] Gregory A. Zimmerli, Marius Asipauskas, et al., Empirical Correlations for the Solubility of Pressurant Gases in Cryogenic Propellants, Cryogenics () (2010).

[31] Van P. Carey, Boiling and Condensation Heat Transfer, Taylor & Francis Group, New York, NY, 2008.

[32] L.A. Weber, Thermodynamic and Related Properties of Oxygen from the Triple Point to 300K at Pressures to 1000 Bar, NASA Reference Publication 1011, National Bureau of Standards, Boulder, CO, 1977.

[33] Randall F. Barron, Cryogenic Systems, 2nd Edition, Oxford University Press, Oxford, 1985.

[34] R.T. Jacobsen, R.B. Stewart, Thermophysical Properties of Nitrogen From The Fusion Line To 3500 R For Pressures To 150,000 PSIA, NBS Technical Note 648, National Bureau of Standards, Boulder, Colorado, 1973.